

# Invertible Neural Networks for Graph Prediction

Chen Xu<sup>\*1</sup>, Xiuyuan Cheng<sup>†2</sup>, and Yao Xie<sup>‡1</sup>

<sup>1</sup>H. Milton Stewart School of Industrial and Systems Engineering, Georgia Institute of Technology.

<sup>2</sup>Department of Mathematics, Duke University

## Abstract

In this work, we address conditional generation using deep invertible neural networks. This is a type of problem where one aims to infer the most probable inputs  $X$  given outcomes  $Y$ . We call our method *invertible graph neural network* (iGNN) due to the primary focus on generating node features on graph data. A notable feature of our proposed methods is that during network training, we revise the typically-used loss objective in normalizing flow and consider Wasserstein-2 regularization to facilitate the training process. Algorithmic-wise, we adopt an end-to-end training approach since our objective is to address prediction and generation in the forward and backward processes at once through a single model. Theoretically, we characterize the conditions for identifiability of a true mapping, the existence and invertibility of the mapping, and the expressiveness of iGNN in learning the mapping. Experimentally, we verify the performance of iGNN on both simulated and real-data datasets. We demonstrate through extensive numerical experiments that iGNN shows clear improvement over competing conditional generation benchmarks on high-dimensional and/or non-convex data.

## 1 Introduction

We are interested in the problem of finding an invertible neural network  $g$ , such that given a  $Y$  subject to  $Y = g(X)$  for an input  $X$ , we can find the corresponding  $X = g^{-1}(Y)$ . In particular, this can be viewed as a type of inverse problem. Inverse problem can be largely categorized as either one-to-one (i.e.,  $Y = g(X)$  with an one-to-one mapping  $g$ ) or can allow for one-to-many mapping

---

<sup>\*</sup>Emails: cxu310@gatech.edu

<sup>†</sup>xiuyuan.cheng@duke.edu

<sup>‡</sup>yao.xie@isye.gatech.edu

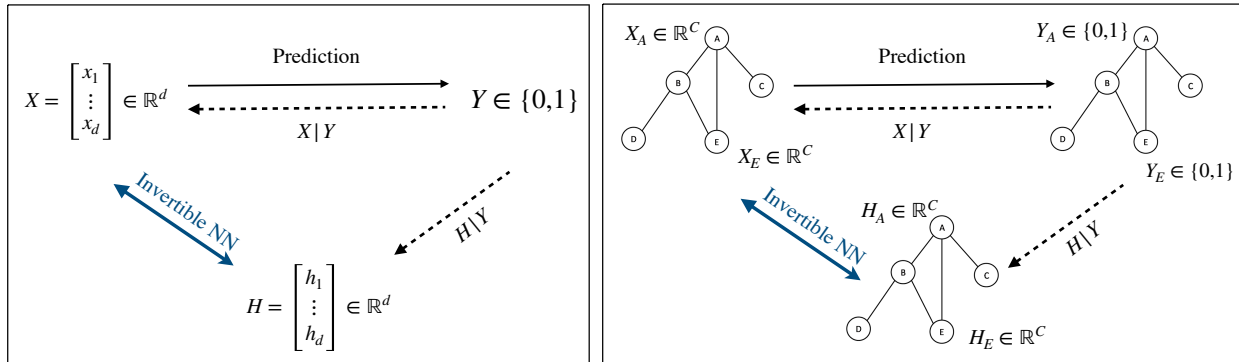


Figure 1: How iGNN applies to non-graph (left) and graph (right) observations. The dashed lines indicate one-to-many mapping from  $Y$  to either  $X|Y$  or  $H|Y$ . In our approach,  $H|Y$  is first generated before mapping through an invertible NN to  $X|Y$ . As a practical example, suppose the graph on the right subfigure is a power grid, where each node  $i \in \{A, \dots, E\}$  denotes a power generator, each  $X_i \in \mathbb{R}^C$  denotes historical power outputs from generator  $i$ , and each  $Y_i \in \{0, 1\}$  denotes whether generator  $i$  is functioning normally (e.g.,  $Y_i = 0$ ) or abnormally (e.g.,  $Y_i = 1$ ). For system monitoring, it is important to both *predict* (indicated by solid black arrows) the status of generators given historical observations and *generate* (indicated by dashed black arrows) possible circumstances (e.g., values on all generators) based on generator status for cause analyses.

(i.e.,  $Y$  is categorical and  $X \in \mathbb{R}^d$ , where  $d$  denotes the number of features). This work focuses on the latter (i.e., we do not necessarily need one-to-one invertible mapping), which naturally arises in many applications. In molecular design (Sánchez-Lengeling & Aspuru-Guzik, 2018), scientists want to infer features of the molecule that lead to certain outcomes (e.g., type of disease). In anomaly detection (Zong et al., 2018) such as power outage detection (Al-Shaalan, 2019), studying distributions of normal vs. anomalous features (e.g., weathers or past power output by sensors) is important for future prevention. In market analysis (Lu et al., 2015), estimating patterns of customers based on their behaviors is crucial for the accurate recommendation. Figure 1 illustrates how our iGNN applies to generic Euclidean and non-Euclidean (e.g., graph) data, which subsume these application examples above.

This one-to-many task is synonymous with conditional generation, where the goal is to generate  $X|Y$  based on specific outcomes  $Y$ . Before introducing common approaches in conditional generation, we acknowledge several (unconditional) generation approaches, which address the simpler question of generating samples as close to features  $X$  as possible. At present, generative adversarial networks (GAN) (Goodfellow et al., 2014; Gulrajani et al., 2017) and variational auto-encoders (VAE) (Kingma & Welling, 2014, 2019) are two of the most widely studied and popular frameworks. Both approaches have created remarkable successes in many fields (Makhzani et al., 2015; Zhu et al., 2017; Ledig et al., 2017). However, they also have clear limitations, including

the inability to provide an exact evaluation of data likelihood for new samples and difficulties in training, such as mode collapse (Salimans et al., 2016) and posterior collapse (Lucas et al., 2019).

For our purpose of conditional generation, there have also been several streams of works, with an abstract description presented on the left of Figure 2. In the following, we first summarize the limitations of these methods and the open questions in Section 1.1. Then, we introduce the general structure of the invertible neural network used in our paper. Section 1.2 summarizes our contributions and presents the roadmap for this work.

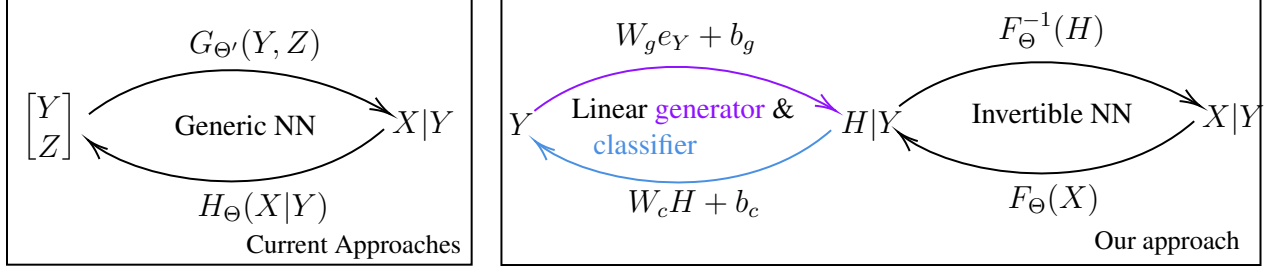


Figure 2: Abstract comparison of (several) current conditional generative models (left) and ours (right). In the forward mapping through  $H_{\Theta}$ , these methods either concatenate  $X, Y$  (Isola et al., 2017; Ardizzone et al., 2019b) or zero-pads  $X$  (Ardizzone et al., 2019a). In the generative procedure through  $G_{\Theta'}$ , both the outcome variable  $Y$  and random noise  $Z$  are taken as network inputs. If the networks are designed to be invertible (Ardizzone et al., 2019b,a), only a single network is needed whereby  $G_{\Theta'} = H_{\Theta}^{-1}$ . These approaches inevitably increase the input and output dimensions of the network, and because  $Y$  and  $Z$  are inherently independent, practical training difficulties often arise. In comparison, our approach maintains the dimensionality of the feature space when training an invertible NN. During generation, we map one-hot-encoded  $Y$  through a simple linear generator onto random vectors  $H|Y$  (whose distributions are disjoint over  $Y$ ) before mapping through the inverse mapping  $F_{\Theta}^{-1}$ . By disjointness,  $H|Y$  allows a simple prediction of  $Y$ .

## 1.1 Background

There have been many studies on conditional versions of GAN (cGAN) (Mirza & Osindero, 2014; Isola et al., 2017), where the outcome  $Y$  and random noise  $Z$  are both taken as inputs to the generator. However, these methods suffer from similar issues as their unconditional counterparts; we would compare iGNN with cGAN in our experiments. More recently, the work (Ardizzone et al., 2019a) directly builds conditional invertible neural networks (CINN) for analyzing inverse problems. A single invertible NN is trained by minimizing maximum mean discrepancy (MMD) losses in the latent space  $Z$  and the original data space  $X$ ; we call their method CINN-MMD for comparison. However, this method also takes in the outcome  $Y$  as an additional input to its invertible NN, thus increasing the dimensionality of the original problem. In addition, the scalability of MMD-based methods in high-dimensional spaces and choices of kernel bandwidths can also limit its practical

performance, as will be shown in the experiments.

In this work, we tackle the question of conditional generation for inverse problems by extending techniques in normalizing flow (Grathwohl et al., 2019; Behrmann et al., 2019; Ziegler & Rush, 2019; Kobyzev et al., 2020; Ardizzone et al., 2019b). Flow-based methods estimate arbitrarily complex densities via the direct maximum likelihood estimation (MLE) approach—they transport original random features  $X$  into more tractable ones (e.g., standard multivariate Gaussian) through invertible neural networks. However, most methods only focus on unconditional generation. More recently, (Ardizzone et al., 2019b) tackles the conditional generative task by combining conditional invertible neural networks (Ardizzone et al., 2019a) with the normalizing flow, a method which we call CINN-Nflow for comparison. Nevertheless, CINN-Nflow suffers from a similar issue as CINN-MMD—by treating  $Y$  as an input, the data dimension is increased so that training is more difficult.

In addition, there have been many architecture designs of the invertible neural network  $F_\Theta$  (see Figure 2, right). Some are based on coupling layers (Dinh et al., 2017) and autoregressive flows (Wehenkel & Louppe, 2019) while others build on residual networks (Behrmann et al., 2019) and ordinary differential equations (Grathwohl et al., 2019). At present, we choose  $F_\Theta$  to be an invertible *residual network* (iResnet), due to its expressiveness and efficiently-generated inverses as proposed in (Behrmann et al., 2019). Denote  $F_{b,\Theta_b} : \mathbb{R}^C \rightarrow \mathbb{R}^C$  as the  $b$ -th *residual block* with its own trainable parameters  $\Theta_b$ , which has the form

$$F_{b,\Theta_b}(x) := x + g_{b,\Theta_b}(x), \quad (1)$$

$$g_{b,\Theta_b} := W_{b_l} \circ \phi_{b_l} \circ \dots \phi_{b_1} \circ W_{b_1}, \quad (2)$$

where each pair of  $\{W_{b_i}, \phi_{b_i}\}$  in (2) denotes the weight matrix and the activation function at the  $i$ -th layer of the  $b$ -th residual block. Then,  $F_\Theta := F_{B,\Theta_B} \circ \dots \circ F_{1,\Theta_1}$  is the concatenation of  $B$  residual blocks. To ensure invertibility of each block, (Behrmann et al., 2019) suggested using spectral normalizing so that the Lipschitz constant of each  $g_{b,\Theta_b}$  is less than one. However, spectral normalization is computationally expensive and may not be sufficient beyond fully-connected layers, so that we propose an alternative regularization technique in Section 2.3.

Therefore, although conditional generation has been a long-standing and actively researched area, there are still several open questions.

1. *How to design (graph) generative models that do not increase difficulties in training?* Treating  $Y$  as additional inputs increase the data dimension. For non-invertible networks such as cGAN and its variants, doing so requires even more careful hyperparameter tuning and tends to cause



many practical issues, as described earlier. For invertible networks such as CINN-MMD or CINN-Nflow, doing so causes more scalability issues in higher dimensions due to their training objectives. In addition, conditional node feature generation on graph without these training difficulties has not been well-addressed.

2. *How to reformulate the training objective in a natural way that also allows for prediction?*

Most conditional generative models consider the same loss as their unconditional counterparts and mainly differ by taking in  $Y$  as network inputs. In addition, for prediction, these models either require building separate supervised networks or require  $Y$  as an additional output by the generative model (e.g., CINN-MMD). Both of these approaches increase complexities in training.

## 1.2 Contribution

Compared to current approaches (see Figure 2, left), our approach (see Figure 2, right) circumvents the inevitable dimensionality issue: we first generate hidden variables  $H|Y$  that have *disjoint* supports over  $H$  and then trains a single invertible network that maintains the original data dimension. Due to disjointness, the prediction of  $Y$  can also be performed by simple linear classifiers. The method is called *invertible graph neural network* (iGNN) due to our primary focus on graph data. In summary, our technique contributions in response to the open questions above include

1. For the training objective, we formulate a conditional generative loss based on the change-of-variable formula (see Eq. (3)), which naturally extends to graph observations (see Eq. (7)). Predicting the outcome  $Y$  is simple based on our problem design and is built as a part of our end-to-end training. In particular, the invertible neural network does not treat the conditional variable  $Y$  as an additional network input to maintain the original data dimension.
2. In network design, we impose the Wasserstein-2 regularization on each residual block of the invertible residual network in iGNN. In contrast to the much more expensive spectral normalization (Behrmann et al., 2019), this regularization is easy-to-implement and facilitates smoother density transport.
3. Theoretically, we establish the identifiability of a true invertible mapping and verify its existence and invertibility based on the well-posedness of the initial-value problem for ordinary differential equations. We also show that graph neural networks with enough (resp. insufficient) expressiveness can (resp. cannot) theoretically learn the true invertible mapping.

4. In experiments, we compare the performance of our model with competing models on simulated and real data, with clear improvement over competing models on high-dimensional and/or non-convex graph data. We also verify the importance of model expressiveness through specific simulation designs.

The rest of the paper is organized as follows. Section 2 contains our method. We describe how the training objective is formulated to include prediction and conditional generation, how the framework is extended to graph data, and how each residual block is regularized through the Wasserstein-2 penalty. Section 3 contains theoretical analyses with three parts. We first establish the identifiability of the true invertible mapping, assuming its existence. Then, we analyze when such invertible mappings exist upon connecting with ODE. Lastly, we derive a closed-form expression for the invertible mapping in a special case and consider the expressiveness of our iGNN in two examples. Section 4 contains simulated and real-data experiments, which show the improved performance of our method over other conditional generative models, especially when data are high-dimensional and/or non-convex. In particular, we also verify the model expressiveness statements in Section 3 with numerical results. Section 5 concludes our work and discusses future directions. Section 6 contains complete derivation and proofs. Appendix A contains details regarding experiment setups and additional numerical results.

## 2 Method

We first describe how the training objective is formulated in Section 2.1 for generic Euclidean data. We then discuss the extension to non-Euclidean data, such as graph observations in Section 2.2. Lastly, we propose the regularization technique of residual blocks described in (2) in Section 2.3.

### 2.1 End-to-end training for conditional generation and prediction

We now present the concrete mathematical formulation of our training objective based on the abstract representation on the right of Figure 2. Compared to other conditional generative models, our iGNN performs a simple but effective modification of the unconditional generative loss based on the change-of-variable formula. As we will see, doing so has several benefits: (1) maintain the original data dimension of  $X$  instead of increasing it to include  $Y$ , (2) facilitate model training as the network only needs to transport each  $X|Y$  to its corresponding  $H|Y$  instead of all  $X|Y$  to a standard Gaussian variable  $Z$ , and (3) enable easy classification, as each  $H|Y$  is designed to be

disjoint.

We first consider the case where the random feature  $X \in \mathbb{R}^d$ . Given an invertible network  $F_\Theta$  and additional categorical outcome variables  $Y \in [K]$  for  $K$  classes, we consider the following conditional generative loss:

$$\begin{aligned}\log p_{X|Y}(X) &= \log p_{H|Y}(F_\Theta(X)) + \log |\det J_{F_\Theta}(X)|, \\ L_g &:= -\log p_{X|Y}(X),\end{aligned}\tag{3}$$

where  $L_g$  denotes the generative loss to be minimized and each  $H|Y$  is disjoint over the value of  $Y$ . Note that conditional generation based on (3) is simple—given different outcomes  $Y$ , we can sample from different distributions  $H|Y$  and then perform the inverse mapping  $F_\Theta^{-1}$ . In implementation, we let distributions  $H|Y$  be isotropic multivariate Gaussian distributions, with mean parameters  $\mu(H|Y) := W_g e_Y + b_g$  using trainable parameters  $\{W_g, b_g\}$  and variances to be small enough for disjointness. The term  $e_Y$  denotes the  $Y$ -th standard basis vector in  $\mathbb{R}^K$ , and the subscript  $g$  denotes generation.

While the loss in (3) may seem simple, we highlight its benefit over the current CINN-Nflow approach (Ardizzone et al., 2019b), whose loss is also based on the change-of-variable formula. CINN-Nflow treats  $Y$  as the network input and writes

$$\begin{aligned}\log p_{X|Y}(X) &:= \log p_Z(G_{\Theta'}(X, Y)|_Z) + \log |\det J_{G_{\Theta'}}(X, Y)|, \\ G_{\Theta'}(X, Y) &:= [G_{\Theta'}(X, Y)|_Y, G_{\Theta'}(X, Y)|_Z]. \quad (\text{Dimension increase})\end{aligned}\tag{4}$$

In (4),  $Z$  denotes a standard multivariate Gaussian random vector and  $G_\Theta$  is the conditional invertible neural network. In contrast to our objective (3), the output  $G_{\Theta'}(X, Y)$  in (4) contains predictions for *both*  $Y$  and  $Z$ , so that the dimension of the original feature space is increased. In addition, because  $Z$  and  $Y$  are inherently *independent*, the conditional generative model  $G_{\Theta'}^{-1}$  must transport the uni-modal random vector  $Z$  into multiple  $X|Y$ , each of which may be multi-modal. Both procedures increase the difficulty in training.

In addition, our conditional formulation in (3) also allows one to perform classification (e.g., estimate  $Y|X$ ) using simple classifiers. For instance, assuming  $Y$  is binary but the original decision boundary of  $Y|X$  is highly nonlinear. Instead of relying on complex classifiers (e.g., another supervised neural network), one may build a simple one (e.g., linear classifier) as long as (1) distributions  $H|Y$  do not overlap (e.g., disjoint multivariate Gaussian distributions) (2) the invertible mapping can accurately transport the distribution of  $X|Y$  to match that of  $H|Y$ . Mathematically,

we thus minimize the classification loss using a simple linear classifier on  $F_\Theta(X)$ :

$$\mathcal{L}_c := \mathcal{L}(Y, W_c F_\Theta(X) + b_c) = -e_Y^T \text{softmax}(W_c F_\Theta(X) + b_c). \quad (5)$$

Therefore, our end-to-end training objective can be written as

$$\min_{\{\Theta, \{W_c, b_c\}, \{W_g, b_g\}\}} \mathbb{E}_{X,Y} [\mathcal{L}_g + W_2(F_\Theta) + \mu \mathcal{L}_c], \quad (6)$$

which is estimated using training data. The term  $W_2(F_\Theta)$  will be introduced in Section 2.3, Eq. (8) to ensure model invertibility and smoothness in density transport. The term  $\mu$  is a parameter that controls the relative rate at which the generative model trains with respect to the linear classifier. In practice,  $\mu$  can be chosen small because of problem formulation—classification is easy as long as estimated distributions using  $F_\Theta(X)|Y$  accurately match those of  $H|Y$ , which are disjoint. Figure 3 illustrates the result on a simple simulated two-moon data. For prediction, both parts of the two-moon data are mapped separately through the invertible map to disjoint parts of the Gaussian mixture, which can be easily classified via the linear classifier  $x = y$ . For conditional generation, one simply samples from the Gaussian mixture, and the invertible map  $F_\Theta^{-1}$  generates the desired  $X|Y$ .

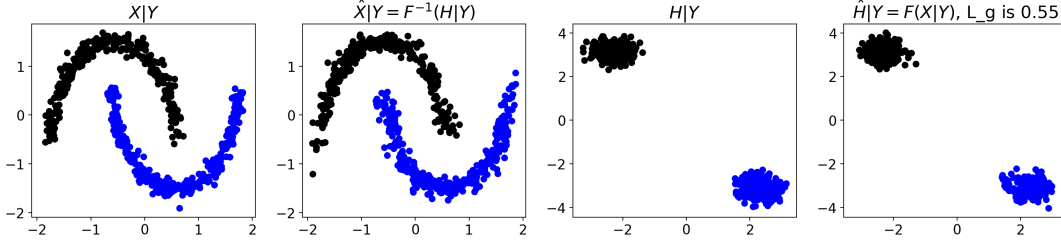


Figure 3: Illustration of iGNN on a toy example. We compare  $X|Y$  vs.  $\hat{X}|Y := F_\Theta^{-1}(H|Y)$  and  $H|Y$  vs.  $\hat{H}|Y := F_\Theta(X|Y)$ , where the estimates are very close to the true conditional distributions.

## 2.2 Generative loss on graph data

A key emphasis of our paper is on non-Euclidean observation, such as graph data, where we currently focus on node classification and node feature generation. Notation-wise, given a graph  $G = (V, E)$  with  $|V| = V$  (with a slight abuse of notation), let  $A$  be its adjacency matrix,  $D_A$  be the degree matrix,  $X^{(v)} \in \mathbb{R}^C$ ,  $v = 1, \dots, V$  be the node feature, and  $Y^{(v)} \in [K]$  be the node label. Denote  $X \in \mathbb{R}^{V \times C}$  as the matrix of node features and  $Y \in \{1, \dots, K\}^V$  as node labels.

For training, we still minimize the end-to-end objective in (6). However, there is a key difference

regarding the evaluation of the log-likelihood of input node features  $X$ :

$$\begin{aligned}
& \log p_{X|Y}(X) \\
&= \log p_{H|Y}(F_{\Theta}(X)) + \log \det J_{F_{\Theta}}(X) && \text{(Change of variable)} \\
&\stackrel{(i)}{=} \sum_{v=1}^V \left[ \log p_{H^{(v)}|Y^{(v)}}(F_{\Theta}(X)^{(v)}) \right] + \log \det J_{F_{\Theta}}(X) && \text{(Independence)} \\
&\stackrel{(ii)}{=} \sum_{v=1}^V \left[ \log p_{H^{(1)}|Y^{(1)}}(F_{\Theta}(X)^{(v)}) \right] + \log \det J_{F_{\Theta}}(X), && \text{(Homogeneity)} \tag{7}
\end{aligned}$$

where in (i), we assume independence of node features upon transporting the raw feature, and in (ii), we further assume that the conditional distribution  $H^{(v)}|Y^{(v)}$  at each node is *homogenous*, so the distribution only depends on the label of  $Y^{(v)}$  rather than the node  $v$ . In practice, requiring (ii) is important as the number of nodes is often significantly larger than the number of node classes. In that case, it is nearly infeasible to pre-specify node-dependent disjoint conditional distributions  $H^{(v)}|Y^{(v)}$ . Computationally, we would perform vectorize-then-unvectorize operations of inputs  $X$  and outputs  $F_{\Theta}(X)$  to make sure  $J_{F_{\Theta}}(X) \in \mathbb{R}^{V \cdot C \times V \cdot C}$ .

### 2.3 Invertible flow Resnet with Wasserstein-2 regularization

Recall that we choose  $F_{\Theta}$  in our iGNN as an invertible residual network (see right of Figure 2), which is a concatenation of residual blocks defined in Eq. (2). To ensure network invertibility, instead of performing spectral normalization of the weight matrices in each residual block, we consider the following regularization on the movement of each residual block:

$$W_2(F_{\Theta}) := \frac{1}{2} \sum_{b=1}^B \|g_{b, \Theta_b}(X)\|_2^2. \tag{8}$$

Note that (8) is the Wasserstein-2 regularization (Bolley et al., 2012). Figure 12 in the appendix shows that our model maintains invertibility on both in-distribution and out-of-distribution data using the Wasserstein-2 regularization in (8).

There are several benefits of the Wasserstein-2 regularization compared to the spectral normalization technique (Behrmann et al., 2019). Computationally, the Wasserstein-2 penalty can be easily implemented as the network performs forward passes on data. In contrast, spectral normalization relies on the power iteration at *each training epoch* to normalize the spectral norm of weight matrices in *all* residual blocks. Doing so can be very computationally expensive when both the total number of residual blocks and the number of hidden neurons are large, whereby the procedure

must spectrally normalize many high-dimensional weight matrices. In addition, the Wasserstein-2 penalty is agnostic of the residual block design—each block can consist of only fully-connected (FC) layers or generic graph filters (Defferrard et al., 2016; Cheng et al., 2021). In contrast, spectral normalization is applicable when each residual block concatenates fully-connected layers (FC) with contractive nonlinearities (e.g., ReLU, ELU, Tanh). When each residual block contains more than FC layers (e.g., general graph filters), it can be insufficient to require the spectral norm of all weight matrix parameters to be less than one.

### 3 Theory

We provide several theoretical results in this section. First, we show in Section 3.1 that under idealized assumptions, the optimal solution of the conditional generative loss (3) identifies the true invertible mapping that generates  $X|Y$  for each  $H|Y$ . Then, we show in Section 3.2 that the true invertible mapping exists under the well-posedness of an ordinary differential equation, which can be verified under certain Lipschitz conditions. Lastly, we discuss in Section 3.3 the expressiveness of our iGNN for Gaussian processes in two examples that depend on graph topology. Throughout this section, we assume that  $X_t \in \mathbb{R}^d$ , where graph features  $X_t \in \mathbb{R}^{V \times C}$  can be equivalently interpreted as random vectors in  $\mathbb{R}^{V \cdot C}$ , with correlation among features according to the graph structure. All derivatives and proofs appear in Appendix 6.

#### 3.1 Identifiability

Upon minimizing  $L_g$  in (3), we first have the following proposition regarding the identifiability of a true invertible mapping  $F^*$ .

**Proposition 3.1** (Identifiability of the true mapping). *Let  $Y \in \{1, \dots, K\}$  be discrete labels. Assume that*

- *For any  $i, j \in [K]$  with  $i \neq j$ , the random vectors  $H|Y = i$  and  $H|Y = j$  follow disjoint tractable distributions (e.g., multivariate Gaussian).*
- *There exists a bijective mapping  $F^* : \mathbb{R}^d \rightarrow \mathbb{R}^d$  such that for every  $i \in [K]$ ,  $\hat{H}_i := F^*(X|Y = i)$  follows the same distribution as  $H|Y = i$ .*
- *There exist parameters  $\Theta^*$  such that  $F_{\Theta^*} = F^*$ , where  $F_{\Theta} : \mathbb{R}^d \rightarrow \mathbb{R}^d$  is the pre-specified class of invertible models that depends on parameters  $\Theta$ .*

Based on (3), denote

$$\begin{aligned}\hat{\Theta}_N &:= \arg \max_{\Theta} \sum_{n=1}^N \log p_{H|Y}(F_{\Theta}(X_n)) + \log |\det J_{F_{\Theta}}(X_n)|, \\ N_K &:= \min_{i=1,\dots,K} \sum_{n=1}^N \mathbf{I}(Y_n = i),\end{aligned}\tag{9}$$

where (9) is the maximum-likelihood estimator based on  $N$  independent and identically distributed (upon conditioning on values of  $Y$ ) samples  $\{(X_n, Y_n)\}_{n=1}^N$ . Then, under regularity conditions for maximum likelihood estimation, we have that as  $N_K \rightarrow \infty$ ,  $\hat{\Theta}_N \rightarrow \Theta^*$  with probability 1.

### 3.2 Existence and invertibility

Note that Proposition 3.1 relies on the idealized assumption that there exists a true invertible mapping  $F^*$  that transports  $X|Y$  to  $H|Y$  as desired. In this subsection, we utilize the Fokker-Planck equation of an Ornstein-Uhlenbeck (OU) process to show that such an invertible mapping exists and can be approximated by a residual network with finite model complexity.

We first reduce the problem to the construction of invertible flow for the unconditional case. The conditional case can be viewed as having a *joint* flow which coincides with each individual flow upon restricting to the support of  $p_{X|Y}$ . More precisely, this joint flow maps each  $p_{X|Y}$  to its corresponding  $p_{H|Y}$ , all of which are disjoint over  $Y$ ; disjointness can be achieved by re-scaling and shifting of a standard Gaussian (see explanation earlier below Eq. (3)). As a result, once the existence of invertible flow from some  $p_X$  to a normal random vector can be constructed, then composed with the shifting and re-scaling operations which are invertible transports, one can construct an invertible joint flow for the conditional generating of  $X|Y$ .

Below, we consider the unconditional case where the desired flow transports from data distribution  $p_X$  in  $\mathbb{R}^d$  to a normal distribution  $p_H$  which is  $\mathcal{N}(0, I_d)$ . Recall that the continuous-time flow is represented by an initial value problem (IVP) of ODE

$$\frac{dx_t}{dt} = \mathbf{f}(x_t, t),\tag{10}$$

with initial value  $x_0 \sim p_X$ . The solution mapping  $x_t := P_t(x_0)$  for  $t > 0$  is invertible as long as (10) is well-posed. There may be more than one  $\mathbf{f}(x, t)$  which induces such a flow towards  $p_H$ , and to show existence, we construct  $\mathbf{f}$  to correspond to the following Fokker-Planck equation of an OU

process ( $\nabla$  denotes  $\nabla_x$ )

$$\partial_t \rho = \nabla \cdot (\rho \nabla V + \nabla \rho), \quad V(x) = \frac{|x|^2}{2}, \quad \rho(x, 0) = p_X(x), \quad (11)$$

where  $\rho(x, t)$  represents the probability density of the OU process at time  $t$  starting from  $\rho(x, 0)$ . Comparing (11) to the Liouville equation of (10) which is  $\partial_t \rho = -\nabla \cdot (\rho \mathbf{f})$ , where  $\rho(x, t)$  represents the distribution of  $x_t$ , we see that the density transportation under the flow can be made the same as in (11) if we set the force  $\mathbf{f}$  as

$$-\mathbf{f}(x, t) = \nabla V(x) + \nabla \log \rho(x, t) = x + \nabla \log \rho(x, t). \quad (12)$$

We first show the differentiability of  $\mathbf{f}(x, t)$  in the following lemma.

**Lemma 3.2.** *Suppose  $\rho(x, t)$  is the solution to (11) from  $\rho(x, 0) = p_X$ , then  $\mathbf{f}(x, t)$  as in (12) is smooth on  $\mathbb{R}^d \times (0, \infty)$ .*

The following proposition directly gives the well-posedness of the IVP, and subsequently the invertibility of the continuous-time flow, assuming an  $x$ -Lipschitz constant of  $\mathbf{f}(x, t)$ . The  $x$ -derivative of a vector field  $\mathbf{v}(x)$  is denoted as  $\nabla \otimes \mathbf{v}(x)$  which is a  $d$ -by- $d$  matrix and we use  $\|\cdot\|$  to stand for matrix operator norm.

**Proposition 3.3.** *Suppose  $\mathbf{f}(x, t)$  as in (12) with  $\rho(x, t)$  being the solution to (11) satisfies that*

$$\|\nabla \otimes \mathbf{f}(x, t)\| \leq L, \quad \forall t > 0, \quad x \in \mathbb{R}^d,$$

*then the IVP (10) is well-posed.*

The boundedness of the  $x$ -Lipschitz constant of  $\mathbf{f}(x, t)$  can be shown when the initial distribution  $\rho(x, 0)$  is sufficiently regular and decay fast on  $\mathbb{R}^d$ , e.g., smooth and compactly supported. The precise analysis is deferred to future work. Under generic conditions, the solution  $\rho(x, t)$  of Fokker-Planck equation converges to the equilibrium distribution  $\rho_\infty \propto e^{-V}$  exponentially fast under e.g.  $L^2$  or Wasserstein-2 distance (Bolley et al., 2012). This means that at time  $T \sim \log \frac{1}{\epsilon}$ , the transported distribution of  $x_T$  is  $\epsilon$ -close to the normal density. One can construct a discrete-time flow on  $[0, T]$  to approximate the continuous-time one, and when the force  $\mathbf{f}(x, t)$  is sufficiently regular, at each  $t$  it can be approximated by a residual block with finite many trainable parameters. Furthermore, since the  $x$ -Lipschitz constant of  $\mathbf{f}(x, t)$  is bounded by  $L$ , invertibility of the ResNet can be fulfilled as long as the discrete time-step  $\Delta t < 1/L$ , and the number of residual blocks equals  $T/\Delta t$  which can be made  $\sim TL$ .



### 3.3 Model expressiveness

Above in Section 3.2 that we verified the existence of an invertible mapping and argued for approximation of the force  $\mathbf{f}(x, t)$  in (12) using a residual network with finite model complexity. In this subsection, we further establish the exact form of  $\mathbf{f}(x, t)$  for Gaussian processes (GP). In particular, we discuss two graph cases where the covariance matrix  $\Sigma$  of the initial distribution of the GP directly relates to properties of the graph, with an interesting implication regarding model expressiveness of GNN.

We first provide the following analytic form of  $\mathbf{f}(x, t)$  in (12), which applies to general vector data in  $\mathbb{R}^d$ :

**Lemma 3.4.** *If  $X_0 \sim N(0, \Sigma)$  and  $X_\infty \sim N(0, I_d)$ , then*

$$\mathbf{f}(x, t) = -(I_d - \Sigma_t^{-1})x, \quad (13)$$

where  $\Sigma_t := (1 - \exp(-2t))I_d + \exp(-2t)\Sigma$  is the covariance matrix that converges to  $I_d$  exponentially fast.

Because the force  $\mathbf{f}(x, t)$  in (13) is linear, it can always be approximated by residual blocks of fully-connected layers, which are universal approximators (Haykin, 1998; Lu et al., 2017).

On the other hand, one can interpret the random vector  $X_0$  as the collection of *one-dimensional node features* on a graph with  $d$  nodes, with  $\Sigma$  encoding feature dependency. In such cases, it is not always true that *any* graph filters can approximate  $\Sigma$  and as a consequence, the covariance  $\Sigma_t^{-1}$  in (13) that depends on  $\Sigma$ ; one example that spectral-based GNN fails to do so will be given in Example 1. In particular, we have the following propositions on the properties of  $\Sigma_t$  under different assumptions of  $\Sigma$ , which help us identify networks that are able or unable to approximate the force  $\mathbf{f}(x, t)$ . More precisely, we relate  $\Sigma$  to the spectral-based GNN in one case and spatial-based GNN in another.

For notation consistency with previous discussion on graph data, we change the dimensionality  $d$  to  $V$  in statements on graph data from now on. For simplicity, all analyses onward implicitly assume node features have dimension  $C = 1$ .

*Case I. Spectral-based presentation of  $\Sigma$ :* We first show that when  $\Sigma$  can be written as a polynomial expression of the graph Laplacian  $L$ , then  $\Sigma_t$  has a closed-form in terms of the polynomial evaluated on eigenvalues of the graph Laplacian, whereby  $\Sigma_t^{-1}$  can be approximated up to arbitrary precision by another polynomial. Hence, spectral-based GNN can in theory correctly approximate the true force in (13).

**Proposition 3.5** (Spectral-based  $\Sigma$ ). *Denote  $L \in \mathbb{R}^{V \times V}$  as the graph Laplacian. Suppose there exists a polynomial  $P$  such that  $\Sigma = P(L)$ . Then*

$$\Sigma_t^{-1} = \sum_{i=1}^V ((1 - \exp(-2t)) + \exp(-2t)P(\lambda_i(L)))^{-1} U_i U_i^T,$$

where  $\lambda_i(L)$  denotes the  $i$ -th largest eigenvalue of  $L$  and  $U = [U_1, \dots, U_V]$  with  $L = U \Lambda U^T$  under eigen-decomposition.

The implication of Proposition 3.5 is that under certain regularity condition on  $P$ , there exists another polynomial  $P_t$  that can approximate  $\Sigma_t^{-1}$  up to arbitrary precision. For instance, when  $P$  denotes the Chebyshev polynomial of order  $k$ , then this approximation can be achieved by (possibly) raising the degree of polynomial above  $k$ .

We also consider a corollary below where the covariance matrix  $\Sigma$  is not accurately represented by  $P(L)$ , so that estimation errors exist.

**Corollary 3.6.** *Under the same notations in Proposition 3.5, suppose*

- (1)  $\Sigma$  and  $L$  share the same eigen-bases.
  - (2) For some polynomial  $\tilde{P}$ ,  $\min_i \tilde{P}(\lambda_i(L)) > 0$ , where  $\lambda_i(A)$  denotes the  $i$ -th largest eigenvalue of a matrix.
  - (3) There exists  $\delta > 0$  such that  $\max_i |\lambda_i(\Sigma) - \tilde{P}(\lambda_i(L))| \leq \delta$ .
- Define  $\tilde{\Sigma}_t := (1 - \exp(-2t))I_V + \exp(-2t)\tilde{P}(L)$ . Then

$$\rho(\Sigma_t^{-1} - \tilde{\Sigma}_t^{-1}) = O(e^{-2t}\delta),$$

where  $\rho$  denotes the spectral norm of the matrix difference, and the constant in big- $O$  depends on the minimum eigenvalues of  $\Sigma$  and  $\tilde{P}(L)$ . In particular, note that  $\tilde{\Sigma}_t$  can be approximated up to arbitrary precision based on the implication of Proposition 3.5.

*Case II. Spatial-based presentation of  $\Sigma$ :* We next show that under certain spatial properties of  $\Sigma$ ,  $\Sigma_t^{-1}$  satisfies similar spatial properties and can thus be approximated by spatial-based GNN filters such as the low-rank locally learnable network (L3net) (Cheng et al., 2021). However, it may *not* be approximated by spectral-based GNN such as Chebnet (Defferrard et al., 2016) as shown in Example 1. We first define the desired spatial property in terms of locality.

**Definition 3.7** ( $v$ -locality). Denote  $A \in \mathbb{R}^{V \times V}$  as the graph adjacency matrix for  $d$  nodes. We define that the covariance matrix  $\Sigma \in \mathbb{R}^{V \times V}$ , which encodes correlation among node features, is

$v$ -local for some integer  $v \geq 1$  if

$$\Sigma_{ij} = 0 \text{ if } j \notin \mathcal{N}_i^{(v)},$$

where  $\mathcal{N}_i^{(v)}$  denotes the set of  $v$ -th neighbors of node  $i$  (e.g., all nodes accessible from node  $i$  within  $v$  steps along adjacent nodes).

**Proposition 3.8** (Local  $\Sigma$  and  $\Sigma^{-1}$ ). *Suppose  $\Sigma$  and  $\Sigma^{-1}$  are  $v_1$ -local and  $v_2$ -local based on Definition 3.7. Then depending on values of  $t$ ,  $\Sigma_t^{-1}$  in (13) can be expressed by power series of  $\Sigma$  or  $\Sigma^{-1}$ . If the power series are truncated at order  $k$ ,  $\Sigma_t^{-1}$  can be approximated by a  $\max(kv_1, kv_2)$ -local covariance matrix.*

On the other hand, the following simple example show that spectral-based GNN can never learn  $\Sigma$  and therefore, the covariance  $\Sigma_t^{-1}$  required by the force  $\mathbf{f}(x, t)$  in (13). We will revisit this example in Section 4.3.

*Example 1* ( $\Sigma_t^{-1}$  cannot be learned by spectral-based graph filters). Consider a simple graph with three nodes  $\{1, 2, 3\}$  and two edges  $\{(1, 2), (2, 3)\}$  between nodes. Self-loops at each node are also inserted. Note that the adjacency matrix  $A$  satisfies the property  $\pi A \pi^T = A$ , where  $\pi \in S_3$  is any permutation matrix over graph nodes. Thus, any graph filter  $f[A]$  based on  $A$  satisfies  $\pi f(A) \pi^T = f(A)$ . However, if the covariance matrix  $\Sigma$  and permutation matrix  $\pi$  take the form

$$\Sigma := \begin{bmatrix} 1 & \rho & 0 \\ \rho & 0 & \rho_1 \\ 0 & \rho_1 & 1 \end{bmatrix}, \pi = \begin{bmatrix} 0 & 0 & 1 \\ 0 & 1 & 0 \\ 1 & 0 & 0 \end{bmatrix},$$

then it is easy to see that  $\pi \Sigma \pi^T \neq \Sigma$  if  $\rho \neq \rho_1$ . Therefore, any  $f(A)$  cannot approximate  $\Sigma$  up to arbitrary accuracy.

In summary, Propositions 3.5 and 3.8 state the existence of approximations for  $\Sigma_t$  under correct model specification. In experiments, we will explore the importance of architecture design—whether  $\Sigma_t^{-1}$  can/cannot indeed be approximated by our iGNN under different designs of residual blocks. Results are shown in Section 4.1 Figures 10c (for Proposition 3.5) and 11c (for Proposition 3.8).

## 4 Numerical Examples

The experiments are organized as follows. In Section 4.1, we first compare our iGNN with competing methods on simulated examples, where one of the competitors performs similarly as iGNN. In Section 4.2, we then consider more challenging simulated data and real-data examples.

In particular, the competitors all perform worse than iGNN in terms of conditionally generating the high-dimensional and/or non-convex node features. In Section 4.3, we lastly verify model expressiveness statements in Section 3.3. Code to produce our results can be found at <https://github.com/hamrel-cxu/Invertible-Graph-Neural-Network-iGNN>.

We consider three competing conditional generative models and several two-sample testing metrics for quantitative assessment. Regarding competing methods, we compare iGNN with the conditional generative adversarial network (cGAN) (Isola et al., 2017), the conditional invertible neural network trained with maximum mean discrepancy (CINN-MMD) (Ardizzone et al., 2019a), and the same CINN trained with the normalizing flow (CINN-Nflow) (Ardizzone et al., 2019b). Details and hyperparameters of the competitors in each setting are described in Appendix A.1. Regarding quantitative assessments, two-sample testing statistics are used to compare the similarity between two distributions (e.g.,  $X|Y$  vs.  $\hat{X}|Y$  at different  $Y$ ). In particular, we use kernel MMD under the Gaussian kernel with various bandwidth choices (Gretton et al., 2012) and the energy-based test (Székely & Rizzo, 2013), which utilizes the energy distance or E-statistics for comparisons of distributions. We remark that since CINN-MMD is based on the MMD test (although the kernel functions are different), the kernel MMD statistics can be biased towards this method.

The following settings are fixed in all experiments; other hyperparameters will be explained separately in each experiment. All graphs are assumed undirected and unweighted, with inserted self-loops. The activation function is chosen as ELU (Clevert et al., 2015) due to its continuous derivatives and the hidden dimension is fixed at 64. During training, we use the Adam optimizer (Kingma & Ba, 2015) to minimize the end-to-end objective (6). We terminate the training of all methods once the percentage decrease of training loss is smaller than 0.01%; for compactness and clarity in visualization, we show the training and test losses for competing methods in each experiment in Appendix A.2, Figure 14.

## 4.1 Simple examples

We consider two simulated examples in this section. The first considers non-graph Euclidean vector data, and the second deals with graph node features. In particular, we find that CINN-MMD yields competitive performances as iGNN, but the other two other competing methods perform much worse.

*1. Simulation: 8 Gaussians.* We consider one non-graph toy example that is widely used by conditional generative methods for assessment. Each conditional distribution  $X|Y$  comprises two disjoint Gaussian distributions for four possible choices of  $Y$ . The task is to estimate  $X|Y$  as closely

as possible for each  $Y$ . We build the iGNN to have 40 residual blocks, where each block has four FC layers with 64 hidden nodes. During training, we generate 2500 i.i.d. training and test samples for each of the four labels of  $Y$ , fix the learning rate at  $5e-4$ , and train with a batch size of 1000. Figure 4 compares our generative results with those of CINN-MMD, where both methods can reasonably and correctly estimate each  $X|Y$ . Table 1 provides the two-sample testing statistics, where the values by CINN-Nflow and cGAN are much larger than those by ours and by CIIN: MMD. These larger values indicate a greater discrepancy between the true and estimated conditional distributions.

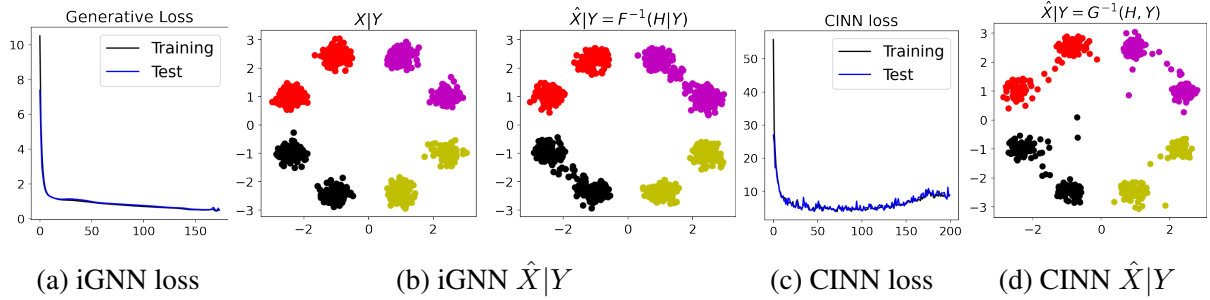


Figure 4: 8 Gaussian visual comparison, iGNN vs. CINN-MMD. Both methods can estimate the true conditional densities  $X|Y$  reasonably well. In addition, we note that while CINN losses increase after approximately 120 epochs, we did not pause the training because generative performances before the loss increase are visually poorer than those after the entire 200 epochs.

Table 1: 8 Gaussian two-sample testing statistics. We considered both the MMD statistics under the Gaussian kernel with various bandwidths (Gretton et al., 2012) and the Energy-based statistics (Székely & Rizzo, 2013). Statistics are weighted by the number of observations at each potential value of  $Y$ . Both CINN-Nflow and cGAN yield much larger test statistics than iGNN and CINN-MMD, indicating a worse estimation of the true conditional distribution.

	MMD: $\alpha = 0.1$	MMD: $\alpha = 1.0$	MMD: $\alpha = 5.0$	MMD: $\alpha = 10.0$	Energy
iGNN	0.001	0.002	0.004	0.003	0.004
CINN-MMD	0.000	0.002	0.004	0.004	0.004
CINN-Nflow	0.367	0.947	0.620	0.460	1.582
cGAN	0.148	0.299	0.273	0.266	0.601

2. *Simulation: 2D convex node features.* We now consider the graph introduced in Example 1. Each node has a binary label so that  $Y \in \{0, 1\}^3$  is a three-dimensional binary vector. Conditioning on a specific binary vector  $Y$  out of the eight choices, the random matrix  $X|Y$  is defined as

$$X|Y := P_A \left( H|Y + \begin{bmatrix} -4 & 0 & 4 \\ 0 & 0 & 0 \end{bmatrix} \right) \text{ s.t. } H^{(v)}|Y^{(v)} \sim \begin{cases} N((1.5, 0)^T, 0.1I_3) & \text{if } Y^{(v)} = 0 \\ N((-1.5, 0)^T, 0.1I_3) & \text{if } Y^{(v)} = 1 \end{cases},$$

where  $P_A := D_A^{-1}A$  is the graph average matrix. In particular, we purposefully design the example so that the marginal distribution of each node feature does not yield enough information for classification (i.e.  $Y^{(v)}$  can be either 1 or zero for the same  $X^{(v)}$ , when features  $X^{(v')}$ ,  $v' \neq v$  remain unobserved). We build the iGNN to have 40 residual blocks, where each block has 3 layers in the form of  $\text{FC} \circ \text{FC} \circ \text{L3net}$  (same neighborhood orders as section 4.1.2). During training, we generate 4000 i.i.d. training and test samples for each of the eight binary vectors  $Y$ , fix the learning rate at  $5 \times 10^{-4}$ , and train with a batch size of 100. Figure 5 shows that the generate and classification performances by our method are both satisfactory, and CINN-MMD can yield similar performances. Meanwhile, Table 2 shows the similar issue that neither CINN-Nflow nor cGAN can yield satisfactory performances.

*Remark 4.1* (Using FC layers on graph data). Note that we can always build each residual block using only FC layers and ignore the relationship among graph nodes. The main difference from using a graph filter is that one has to first vectorize the node feature matrix  $X \in \mathbb{R}^{V \times C}$  as  $\tilde{X} := \text{vec}(X) \in \mathbb{R}^{V \cdot C}$  and then transport the high-dimensional density. Doing so can significantly increase the number of parameters in the model if  $V \cdot C$  is large. Generative performance may also deteriorate in some instances since graph information is ignored.

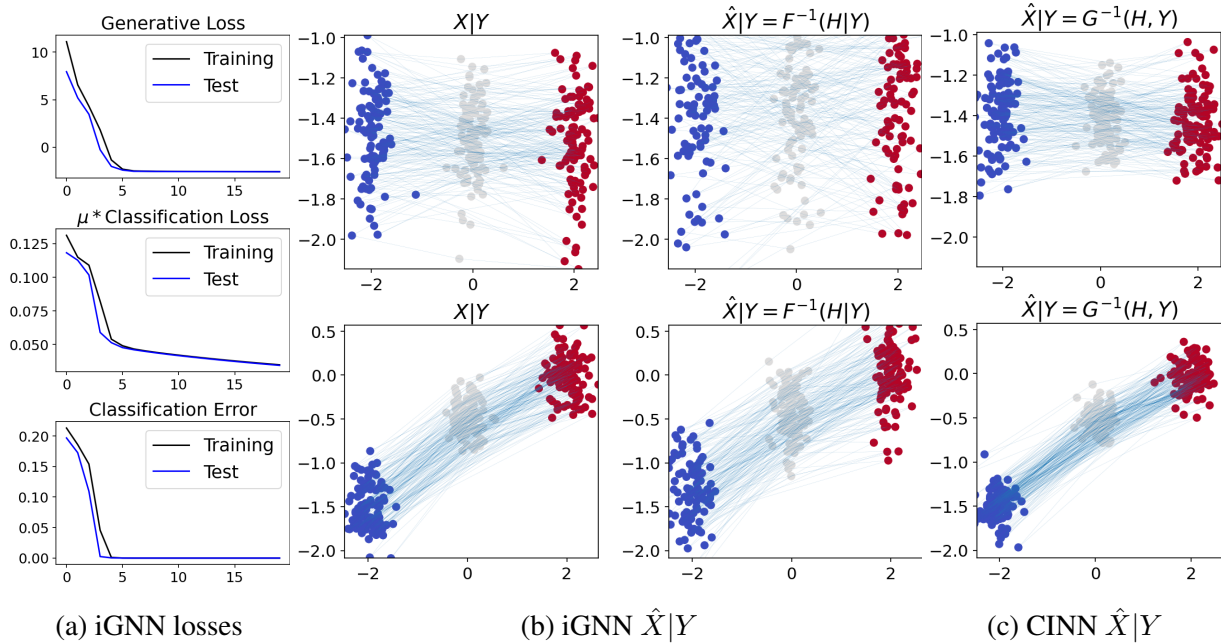


Figure 5: 2D convex node feature visual comparison, iGNN vs. CINN-MMD. We connect in (b) and (c) two-dimensional node features belonging to the same 3-by-2 feature matrix  $X$  by blue lines to reveal the high-dimensional distribution of  $X$ . The conditional generative performances are satisfactory at different values of the random vector  $Y \in \{0, 1\}^3$ . In addition, generative or classification losses and classification errors converge to desired values in a few epochs.

Table 2: 2D convex node feature two-sample testing statistics. Statistics are weighted by the number of observations at each potential value of  $Y$ . Similar to before, neither CINN-Nflow nor cGAN can yield satisfactory performances. Although iGNN yields larger test statistics than that by CINN-MMD, the generative performance in Figure 5 shows that both methods yield similar generative performances.

<b>3 node, convex</b>	MMD: $\alpha = 0.1$	MMD: $\alpha = 1.0$	MMD: $\alpha = 5.0$	MMD: $\alpha = 10.0$	Energy
iGNN	0.007	0.053	0.049	0.027	0.062
CINN-MMD	0.003	0.021	0.032	0.024	0.028
CINN-Nflow	0.749	0.628	0.205	0.087	5.570
cGAN	0.499	1.325	1.181	1.084	2.813

## 4.2 Complex examples

We now consider more challenging node feature generation examples beyond ones in Section 4.1. We first build upon the three-node graph by considering non-convex feature distributions  $X|Y$ . We then consider two high-dimensional real-data graph examples in anomaly detection, where it is essential to generate graph features jointly based on the label at each node (recall Figure 1). In all these cases, we will see that CINN-MMD performs worse than iGNN when node features are non-convex or high-dimensional and that neither CINN-Nflow nor cGAN yields satisfactory performances as iGNN.

*1. Simulation: 2D non-convex node features.* We still use the graph introduced in Example 1 under a more complex node feature setting. At each node  $v$ , features  $X^{(v)}$  can be either convex (e.g., linear transform of Gaussian vectors) or non-convex (e.g., a part of the two-moon dataset as in Figure 3). The response vector  $Y$  is still binary. We ignore details regarding the generation of  $X|Y$ , which is very similar to before, except for the way  $H^{(v)}|Y^{(v)}$  is chosen. We train the same iGNN under the same hyperparameter settings. Figure 6 shows that our method tends to yield better performances when the true conditional distribution is non-convex, which is also verified in Table 3 in terms of the smaller two-sample testing statistics.

Table 3: 2D non-convex node feature two-sample testing statistics. Statistics are weighted by number of observations at each potential value of  $Y$ . The smaller test statistics by iGNN further verify the visual comparisons in Figure 6.

	MMD: $\alpha = 0.1$	MMD: $\alpha = 1.0$	MMD: $\alpha = 5.0$	MMD: $\alpha = 10.0$	Energy
iGNN	0.001	0.006	0.005	0.003	0.008
CINN-MMD	0.003	0.012	0.011	0.007	0.020

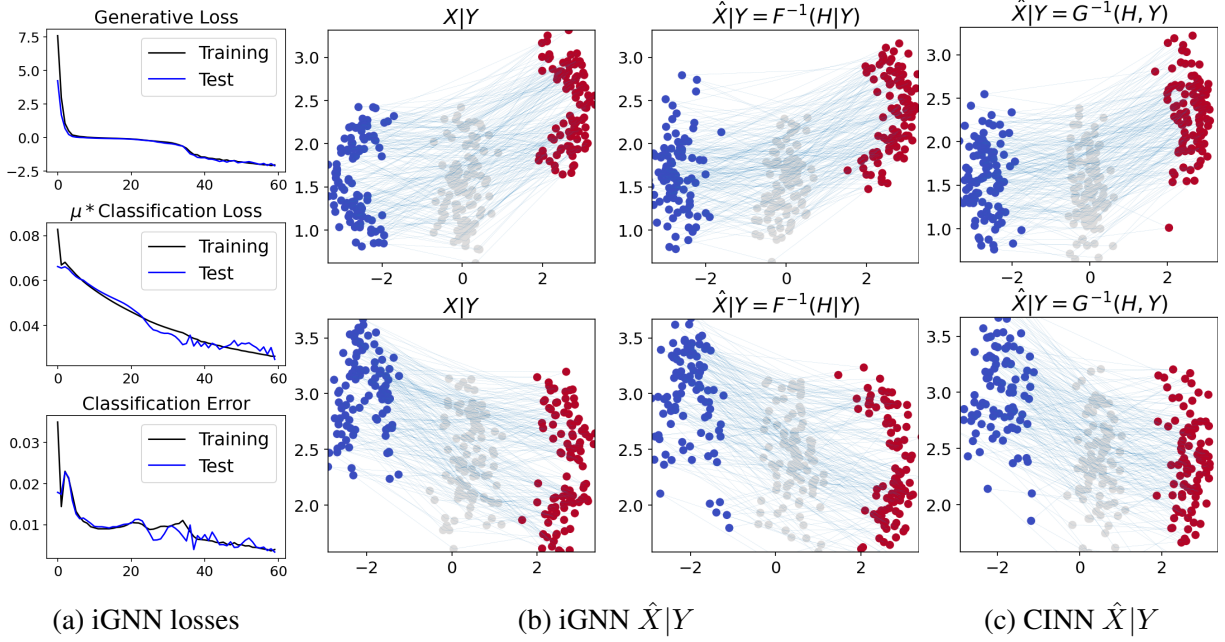


Figure 6: 2D non-convex node feature visual comparison, iGNN vs. CINN-MMD. The setup is nearly identical to Figure 5. The conditional generative performance by iGNN tends to outperform that by CINN-MMD, which fails to capture the non-convexity of feature distributions in some instances.

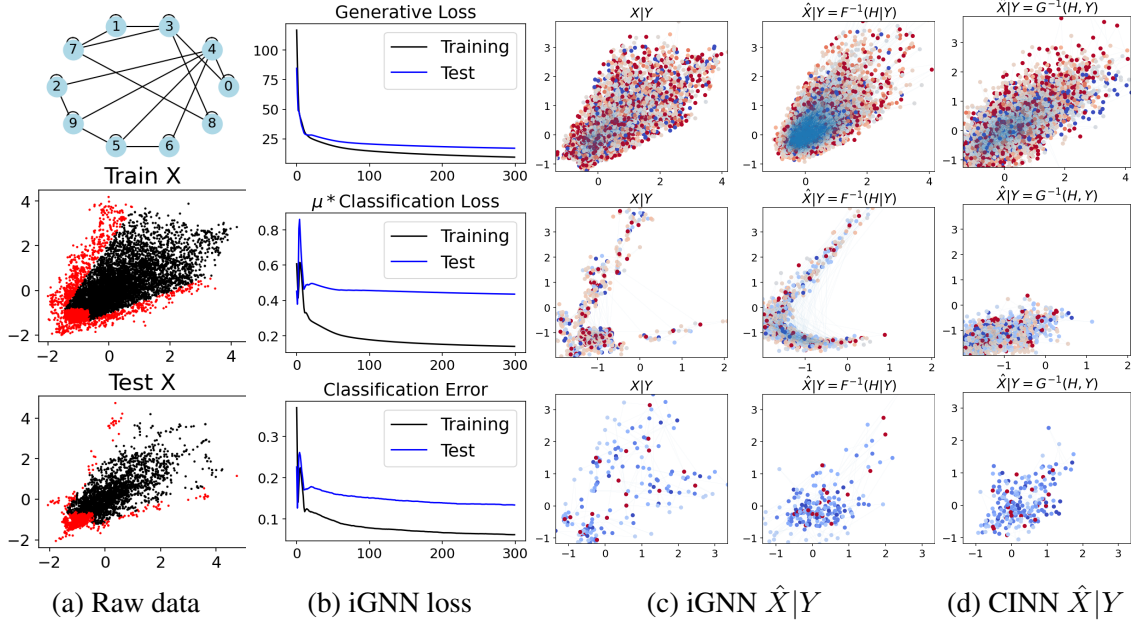


Figure 7: Solar ramping event, visual comparison. We show the network and raw features in (a), loss and error metrics in (b), and generative performances of the 20-dimensional node feature matrices (10 nodes  $\times$  2D features) in (c) or (d), where rows are ordered by values of  $Y \in \{0, 1\}^{10}$  with top three occurrences. We see that the generative performances by ours are satisfactory in general, but CINN-MMD can fail to generate the non-convex distribution  $X|Y$  in the second row of (d).



2. *Real-data: solar ramping events.* We then consider the anomaly detection task on California solar data in 2017 and 2018. The whole network has ten sensors with bi-hourly recordings. Features  $X_t \in \mathbb{R}^{10 \times 2}$  denote the average of raw radiation recordings every 12 hours in the past 24 hours, and response vectors  $Y_t \in \{0, 1\}^{10}$  contain the anomaly status of each city. The first 75% (resp. res 25%) data denote the training (resp. test) data, which have 1094 (resp. 365) graph observations. Figure 7a visualizes the graph and the raw features colored by anomaly status (i.e., black means normal). During training, we fix the learning rate at 1e-4 and train with a batch size of 150. We build iGNN to have 40 residual blocks, where we considered in each block three different architectures: (a) FC  $\circ$  FC  $\circ$  Chebnet of order 2, (b) FC  $\circ$  FC  $\circ$  L3net of neighborhood order (0, 1, 2), and (c) FC  $\circ$  FC  $\circ$  FC. In terms of generative performance, architecture (a) performs the best, whose results are shown in Figure 7 upon comparing with CINN-MMD; we show results for architecture (b) and (c) in Appendix A.2, Figure 15 and 16. In particular, Figure 7 shows that when iGNN captures the entire distributional pattern for different  $X|Y$ , CINN-MMD fails to do so when the underlying distribution is non-convex (see the second row in (c) or (d)). Meanwhile, Table 4 shows that both CINN-Nflow and cGAN yield much larger test statistics than iGNN and CINN-MMD, indicating much poorer generative performance. Although CINN-MMD may yield smaller training statistics than iGNN, the reason is likely attributed to how we weight the statistics for different  $X|Y$  and high variance under insufficient samples. Details can be found in Table 6, Appendix A.2 where we show the test statistics at each  $X|Y$  without weighting.

Table 4: Solar ramping event two-sample testing statistics. Statistics are weighted by the number of observations at each potential value of  $Y$ . Similar to simulation results, CINN-Nflow and cGAN yield much larger test statistics than iGNN and CINN-MMD, indicating much poorer generative performance. The quantitative results by ours and CINN-MMD can be similar, but Figure 7 shows that CINN-MMD cannot accurately predict the distribution  $X|Y$  well when it is non-convex.

<b>Training</b>	MMD: $\alpha = 0.1$	MMD: $\alpha = 1.0$	MMD: $\alpha = 5.0$	MMD: $\alpha = 10$	Energy	<b>Test</b>	MMD: $\alpha = 0.1$	MMD: $\alpha = 1.0$	MMD: $\alpha = 5.0$	MMD: $\alpha = 10$	Energy
iGNN	0.053	0.037	0.010	0.005	0.257	Ours	0.062	0.063	0.014	0.006	0.341
CINN-MMD	0.037	0.039	0.011	0.005	0.197	CINN-MMD	0.061	0.056	0.014	0.006	0.344
CINN-Nflow	0.348	0.067	0.012	0.005	2.907	CINN-Nflow	0.402	0.091	0.015	0.006	3.488
cGAN	0.453	0.874	0.988	0.997	2.683	cGAN	0.572	0.938	0.997	1.000	3.422

3. *Real-data: traffic flow anomalies.* We lastly consider the anomaly detection task on Los Angeles traffic flow data from April to September 2019. The whole network has 15 sensors with hourly

recordings. Features  $X_t \in \mathbb{R}^{15 \times 2}$  denote the raw hourly recording in the past two hours, and response vectors  $Y_t \in \{0, 1\}^{15}$  contain the anomaly status of each traffic sensor. The first 75% (resp. res 25%) data denote the training (resp. test) data, which have 3070 (resp. 1320) graph observations. Figure 8a visualizes the graph and the raw training features, which have different anomaly patterns from the solar ramping events in Figure 7a. During training, we fix the learning rate at  $1e-4$  and train with a batch size of 200. We build iGNN to have 40 residual blocks, where each block contains four FC layers; empirical evidence suggests that combining FC layers with graph filters yields poorer generative performance, which we will examine further in the future. Figure 8 shows that our generative performance is satisfactory in general, whereas CINN-MMD tends to generate distributions much more dispersed than the actual ones. Table 5 further verifies this through the much larger two-sample energy-based test statistics by CINN-MMD.

*Remark 4.2* (Further implications). For many real-world graph datasets, test data may contain node label vectors that lie outside the set of node label vectors in training data, but we can still estimate the distribution of  $X|Y$  upon sampling from  $H|Y$  and applying  $F_{\Theta}^{-1}$ . In words, this tells us “what circumstances (i.e.,  $X$ ) most likely result in (previously unseen) outcomes (i.e.,  $Y$ )”. In the context of anomaly detection on graph, specific nodes may only contain normal observations in training data, but for prognosis, we can examine what features would lead to anomaly outcomes at these nodes.

Table 5: Traffic anomaly detection two-sample testing statistics. Statistics are weighted by the number of observations at each potential value of  $Y$ . Similar to before, both CINN-Nflow and cGAN yield much larger test statistics than iGNN and CINN-MMD, indicating much poorer generative performance. In terms of the energy-based metric, CINN-MMD is also significantly larger than iGNN, coinciding with our observation in Figure 8. Even under the MMD metric on which the objective of CINN-MMD is based, the iGNN can still sometimes reach smaller values.

Training	MMD:	MMD:	MMD:	MMD:	Energy	Test	MMD:	MMD:	MMD:	MMD:	Energy
	$\alpha = 0.1$	$\alpha = 1.0$	$\alpha = 5.0$	$\alpha = 10$			$\alpha = 0.1$	$\alpha = 1.0$	$\alpha = 5.0$	$\alpha = 10$	
iGNN	0.058	0.037	0.010	0.005	0.214	iGNN	0.128	0.059	0.008	0.003	0.537
CINN-MMD	0.140	0.053	0.011	0.005	1.327	CINN-MMD	0.152	0.056	0.008	0.003	1.484
CINN-Nflow	0.316	0.055	0.011	0.005	6.487	CINN-Nflow	0.281	0.058	0.008	0.003	6.183
cGAN	0.823	1.052	1.011	1.005	3.856	cGAN	0.916	1.056	1.008	1.003	4.132

### 4.3 iGNN expressiveness

We focus on verifying model expressiveness analyses in Section 3.3 with empirical evidence. We first revisit the three-node example in Figure 5, where we show that models that *lack expressiveness* can never correctly generate the features. Then, we design two examples according to Propositions 3.5 and 3.8. In the first case, the covariance matrix  $\Sigma$  is similar to the output of a spectral-based graph filter. In the second case,  $\Sigma$  satisfies certain spatial locality properties. We show graph filters that have *enough expressiveness* can accurately estimate the covariance matrix  $\Sigma$  of  $X$  and  $I_d$  of  $H$ , hence transporting the densities correctly.

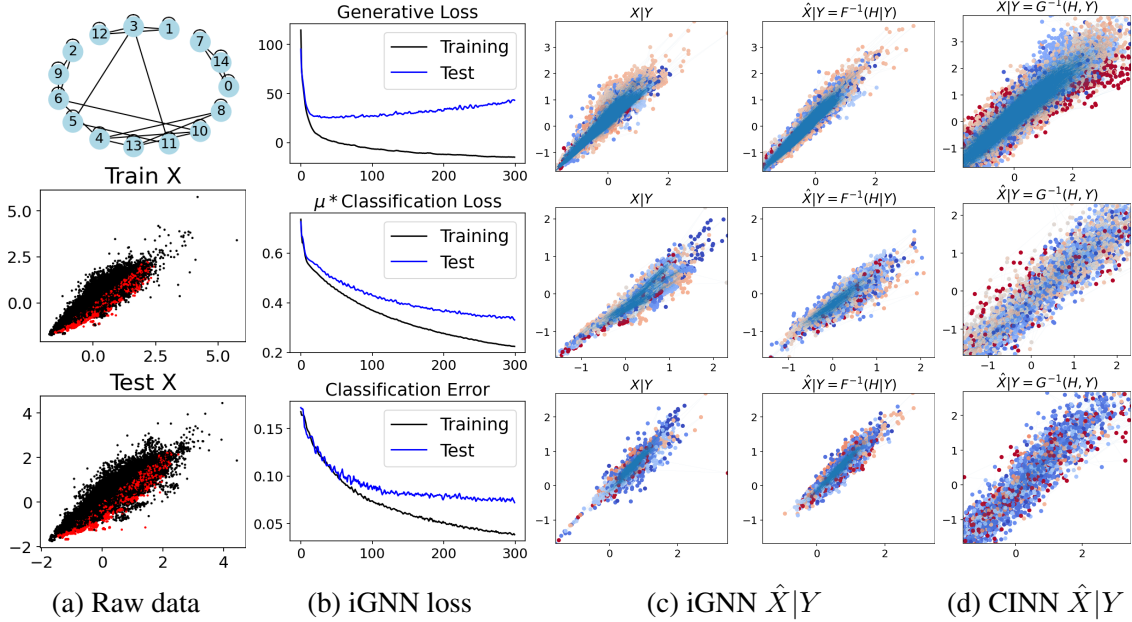


Figure 8: Traffic anomaly detection, visual comparison. We show the network and raw features in (a), loss and error metrics in (b), and generative performances of the 30-dimensional node feature matrices ( $15 \text{ nodes} \times 2\text{D features}$ ) in (c) and (d), where rows are ordered by values of  $Y \in \{0, 1\}^{15}$  with top three occurrences. Our generative performances are generally satisfactory, but CINN-MMD tends to yield much more dispersed distributions even when  $X|Y$  are convex, possibly due to the scalability issue in high-dimensional spaces.

1. *GNN lacks expressiveness.* Recall Figure 5 on the three-node graph in Example 1, where we showed the satisfactory performance of our iGNN. In particular, each residual block takes the form  $\text{FC} \circ \text{FC} \circ \text{L3net}$ . Figure 9 shows the results where we replace the first L3net in each residual block by a Chebnet of order 2 or by a FC layer. In particular, iGNN under the Chebnet variant cannot learn the distribution  $X|Y$ , due to the symmetry issue inherent in spectral-based graph filters mentioned in Example 1.



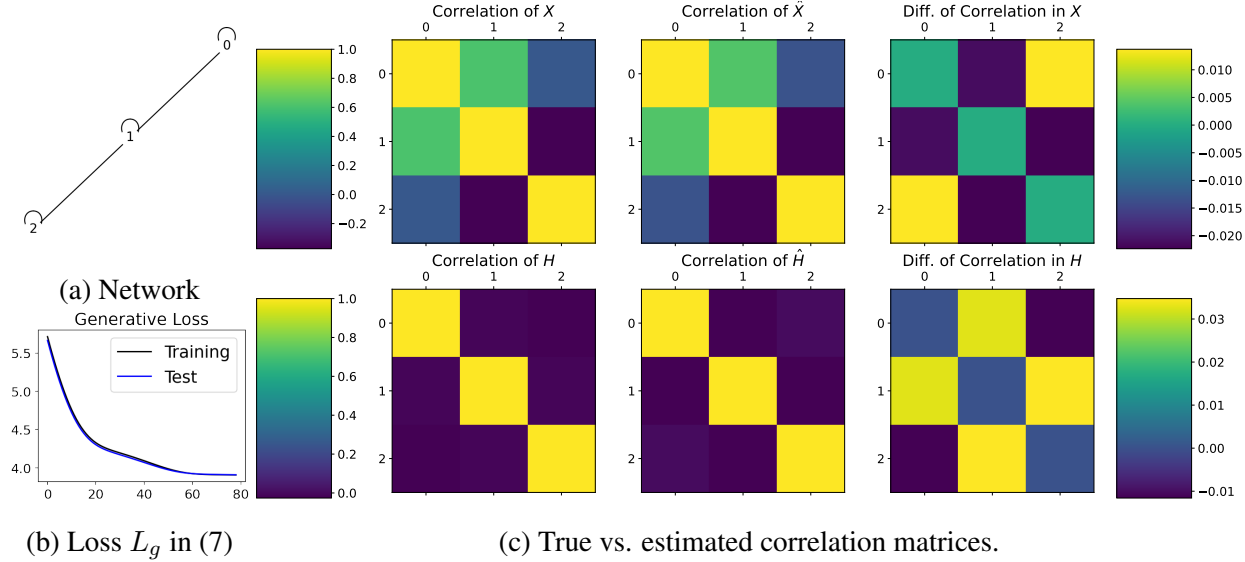


Figure 11: Results for the local  $\Sigma$  as in Proposition 3.8. Losses converge reasonably fast, and correlation matrices are estimated with high accuracy, revealing that iGNN with enough expressiveness can be trained to estimate the true mapping.

2. *Sufficient GNN expressiveness for spectral-based  $\Sigma$ , see Proposition 3.5.* We first consider the case in which  $\Sigma = \sum_{k=0}^2 a_k T_k(\tilde{L})$ , where  $T_k$  denotes the  $k$ -th degree Chebyshev polynomial and  $\tilde{L}$  is the scaled and normalized graph Laplacian. We let  $a_0 = 0.5, a_1 = 0.1, a_2 = 0.5$  so that  $\Sigma$  is positive definite with a significant number of non-zero and large off-diagonal entries. We consider a seven-node chordal cycle graph (Lubotzky, 1994), which is one example of expander graphs. Figure 10a visualizes the raw graph. To verify the existence statement, we design iGNN to have 40 residual blocks, where each residual block is a single Chebnet filter of order two (Defferrard et al., 2016) mapping from  $\mathbb{R}$  to  $\mathbb{R}$ . During training, we generate 4000 i.i.d. training and test samples following the GP, fix the learning rate at  $5e-4$ , and train with a batch size of 400. Figure 10b shows that both the training and test losses converge in a small number of training epochs. Figure 10c shows that the correlation matrices  $\Sigma$  and  $I_V$  are both estimated with high accuracy.

3. *Sufficient GNN expressiveness for spatial-based  $\Sigma$  and  $\Sigma^{-1}$ , see Proposition 3.8.* We then consider the three-node graph in Example 1, where node 1 is connected to both node 0 and 2, neither of which connects each other. In particular, we specify the correlation between node 0 and 1 (resp. 2 and 1) as 0.6 (resp.  $-0.4$ ), so that  $\Sigma$  (resp.  $\Sigma^{-1}$ ) is one-neighbor local (resp. two-neighbor local). Figure 11a visualizes the raw graph. We also use a 40-block iGNN for estimation, where the only difference is that an L3net layer replaces each Chebnet layer with neighborhood orders  $(d_1, d_2, d_3) = (0, 1, 2)$ . All other hyperparameters are the same as those in section 4.1.1 above. Figure 11b shows that the losses converge reasonably fast. Figure 11c shows that the correlation

matrices are estimated with high accuracy. Lastly, note that we intentionally design the correlation matrix  $\Sigma$  to be *asymmetric* as in Example 1, whereas the graph Laplacian is symmetric due to graph design. As a result, any spectral-based graph filter is still unable to express the matrix  $\Sigma$  and, therefore, perform the generative task. Results are shown in Appendix A.2, Figures 13b and 13c, which show that even if losses converge, neither correlation matrices is estimated correctly.

## 5 Conclusion

We proposed a general framework based on normalizing flow for conditional generation in this work. Although our primary focus is on graph data, the framework is general for any Euclidean data, which may be viewed as observations on graphs with a single node, so iGNN naturally applies to these problems. This framework benefits one-to-many inverse problems that aim to infer  $X|Y$ . In particular, our techniques address both prediction and conditional generation through a single invertible residual neural work at once, thus allowing for implementation simplicity and clarity in training. Theoretically, we analyzed the identifiability of a true invertible mapping assuming its existence, verified its existence and invertibility utilizing the Fokker-Planck equation of an Ornstein-Uhlenbeck process, and examined the expressiveness of iGNN in learning the mapping. Experimentally, we compared iGNN with competing conditional generative models on simulated and real-data examples, verifying the improved performance of iGNN, especially in high-dimensional and non-convex graph cases.

There are many open avenues for research. Method-wise, we want to consider continuous outcomes  $Y$  and other generative tasks such as edge feature generation and graph generation. Regarding network training, we want to consider the continuous-time variant of residual networks (Grathwohl et al., 2019) and utilize techniques by monotone variational inequalities in each residual block for performance guarantees (Xu et al., 2022). Theory-wise, we will further the analyses regarding the invertibility of the true force  $\mathbf{f}(x, t)$  in (10) based on the Jordan-Kinderlehrer-Otto (JKO) proximal scheme regularization. We also want to study the expressiveness of iGNN in estimating the true force more deeply.

## Acknowledgement

The work is supported by NSF DMS-2134037. C.X. and Y.X. are supported by an NSF CAREER Award CCF-1650913, NSF DMS-2134037, CMMI-2015787, DMS-1938106, and DMS-1830210. X.C. is partially supported by NSF, NIH and the Alfred P. Sloan Foundation.

## 6 Proofs

*Proof of Proposition 3.1.* Recall that  $F^*$  is bijective in  $\mathbb{R}^d$  and maps  $X|Y$  to  $H|Y$  for each potential value of  $Y$ . Hence, for each value  $i \in [K]$ , the random vector  $\hat{X}_i := F^{*-1}(H|Y = i)$  follows the same distribution as  $X|Y = i$ . Therefore, the random variables generated by the inverse of  $F^*$  follow the same conditional distributions  $X|Y$ . In addition, since we assume that there exists a  $\Theta^*$  at which the model  $F_{\Theta^*}$  is identical to  $F^*$ ,  $F_{\Theta^*}^{-1}(H|Y)$  also follows the true conditional distribution.

By the assumption that  $N_K$  approaches infinity as  $N \rightarrow \infty$ , we know that infinitely many samples from each  $X|Y = i, i \in [K]$  are available. Under additional regularity conditions, we know that the MLE estimate  $\hat{\Theta}_N$  is also consistent (Newey & McFadden, 1986)—it converges to the true parameter  $\Theta^*$  with probability one. Therefore, the model  $F_{\hat{\Theta}_N}^{-1} \rightarrow F_{\Theta^*}^{-1}$  with probability one.  $\square$

*Proof of Lemma 3.2.* The solution  $\rho(x, t)$  of (11) has the explicit expression as

$$\rho(x, t) = \int K_t(x, y) \rho_0(y) dy, \quad K_t(x, y) := \frac{1}{(2\pi\sigma_t^2)^{d/2}} e^{-\frac{|x - e^{-t}y|^2}{2\sigma_t^2}}, \quad \sigma_t^2 := 1 - e^{-2t}. \quad (14)$$

By the smoothness of  $K_t(x, y)$ ,  $\rho(x, t)$  is smooth over  $\mathbb{R}^d \times (0, \infty)$ . By (12), for any  $t > 0$ ,  $\mathbf{f}(x, t) = -x - \frac{\nabla \rho(x, t)}{\rho(x, t)}$ , and thus  $\mathbf{f}(x, t)$  is also smooth over  $\mathbb{R}^d \times (0, \infty)$ .  $\square$

*Proof of Proposition 3.3.* The well-posedness of the IVP can be guaranteed as long as  $\mathbf{f}(x, t)$  is continuous and satisfies a Lipschitz condition w.r.t  $x$  (Sideris, 2013). The former is by Lemma 3.2, and the latter is the assumption of the proposition.  $\square$

*Proof of Lemma 3.4.* We only need to derive the distribution of  $X_t$  in order to find its density function  $\rho(x, t)$ . Because the Ornstein–Uhlenbeck process is a Gaussian process, it is evident that  $X_t \sim N(0, \Sigma_t)$ , where  $\Sigma_t$  is the time-dependent covariance matrix.

By the transition probability, also known as the Green’s function

$$K(X, Y; t) := (2\pi\sigma_t^2)^{-d/2} \exp\left(-\frac{1}{2\sigma_t^2} \|X - \exp(-t)Y\|_2^2\right), \quad \sigma_t^2 := 1 - \exp(-2t),$$

we know that  $X_t|X_0 = Y \stackrel{d}{=} N(0, \sigma_t^2 I_d)$ . When  $X_0 \sim N(0, \Sigma)$ , we thus have

$$X_t = \exp(-t)X_0 + \mathcal{E}, \quad \mathcal{E} \sim N(0, \sigma_t^2 I_d), \quad X_0 \perp \mathcal{E}.$$

Hence,  $\Sigma_t := \text{Var}(X_t) = \exp(-2t)\Sigma + (1 - \exp(-2t))I_d$ .

As a result,  $\rho(x, t) \propto \exp(-1/2 X_t^T \Sigma_t^{-1} X_t)$ , with  $\nabla_X \ln \rho(x, t) = -\Sigma_t^{-1} X_t$ .  $\square$

*Proof of Proposition 3.5.* Note that by the spectral decomposition  $L = U\Lambda U^T$  and the assumption  $\Sigma = P(L)$ , we have

$$\begin{aligned}\Sigma &= \sum_{i=1}^V P(\lambda_i(L)) U_i U_i^T, \\ \Sigma^{-1} &= \sum_{i=1}^V P(\lambda_i(L))^{-1} U_i U_i^T.\end{aligned}$$

Thus,

$$\begin{aligned}\Sigma_t &= (1 - \exp(-2t))I_V + \exp(-2t)\Sigma \\ &= U[(1 - \exp(-2t))I_V + \exp(-2t)P(\Lambda)]U^T.\end{aligned}$$

As a result,

$$\Sigma_t^{-1} = \sum_{i=1}^V ((1 - \exp(-2t)) + \exp(-2t)P(\lambda_i(L)))^{-1} U_i U_i^T.$$

□

*Proof of Corollary 3.6.* By the assumption that  $\Sigma$  and  $L$  share the same eigen-bases, we have

$$\begin{aligned}\Sigma_t &= \sum_{i=1}^V ((1 - \exp(-2t)) + \exp(-2t)\lambda_i(\Sigma)) U_i U_i^T, \\ \tilde{\Sigma}_t &= \sum_{i=1}^V ((1 - \exp(-2t)) + \exp(-2t)\tilde{P}(\lambda_i(L))) U_i U_i^T.\end{aligned}$$

Under diagonalization, the inverse of  $\Sigma_t$  and  $\tilde{\Sigma}_t$  can be expressed as

$$\begin{aligned}\Sigma_t^{-1} &= \sum_{i=1}^V ((1 - \exp(-2t)) + \exp(-2t)\lambda_i(\Sigma))^{-1} U_i U_i^T, \\ \tilde{\Sigma}_t^{-1} &= \sum_{i=1}^V ((1 - \exp(-2t)) + \exp(-2t)\tilde{P}(\lambda_i(L)))^{-1} U_i U_i^T.\end{aligned}$$



Thus, we have

$$\begin{aligned}
& \rho(\Sigma_t^{-1} - \tilde{\Sigma}_t^{-1}) \\
& \leq \max_i | ((1 - \exp(-2t)) + \exp(-2t)\lambda_i(\Sigma))^{-1} - ((1 - \exp(-2t)) + \exp(-2t)\tilde{P}(\lambda_i(L)))^{-1} | \\
& \leq \left| \frac{(1 - c_t)\delta}{(c_t + (1 - c_t)\lambda_d(\Sigma))(c_t + (1 - c_t)\min_i \tilde{P}(\lambda_i(L)))} \right|, \quad c_t := 1 - \exp(-2t).
\end{aligned}$$

Note that the denominator  $(c_t + (1 - c_t)\lambda_d(\Sigma))(c_t + (1 - c_t)\min_i \tilde{P}(\lambda_i(L)))$  is the product of two convex combinations of 1 and either  $\lambda_V(\Sigma)$  or  $\min_i \tilde{P}(\lambda_i(L))$ . Because  $\Sigma$  is positive definite, its minimum eigenvalue is bounded away from zero. Therefore, as long as  $\min_i \tilde{P}(\lambda_i(L)) > 0$ , both  $c_t + (1 - c_t)\lambda_V(\Sigma)$  and  $c_t + (1 - c_t)\min_i \tilde{P}(\lambda_i(L))$  are bounded above and away from zero for all  $t \geq 0$ . Hence, the denominator is bounded above, leading to

$$\rho(\Sigma_t^{-1} - \tilde{\Sigma}_t^{-1}) = O(e^{-2t}\delta),$$

which denotes the tail bound of the spectral norm of the matrix difference.  $\square$

*Proof of Proposition 3.8.* Recall that  $\Sigma_t := (1 - \exp(-2t))I_V + \exp(-2t)\Sigma$ . We thus analyze the locality of  $\Sigma_t$  based on the magnitude of  $t$ .

When  $t = 0$ ,  $\Sigma_t = \Sigma$  so that  $\Sigma_t = \Sigma^{-1}$ .

When  $t > 0$ , we consider two cases:

(1) *Long-time:* Assume  $\exp(-2t) \leq 1/2$  and denote  $c_t := \exp(-2t)/(1 - \exp(-2t))$ . Then,

$$\Sigma_t = (1 - \exp(-2t))[I_V + c_t\Sigma],$$

which yields

$$\Sigma_t^{-1} = (1 - \exp(-2t)) \left[ \sum_{p=0}^{\infty} (-1)^p (c_t \Sigma)^p \right] \quad (15)$$

by the power series expansion  $(I + A)^{-1} = \sum_{p=0}^{\infty} (-1)^p A^p$  if the spectral norm  $\rho(A) < 1$ . We may assume that  $\rho(c_t \Sigma)$  is small enough so that this hold, especially given that  $c_t$  converges to zero exponentially fast.

Therefore, if  $\Sigma$  is local, we can truncate (15) up to the first  $k$  summands. Meanwhile, note that when  $\Sigma$  is  $v_1$ -local,  $\Sigma^k$  is  $kv_1$ -local, as each matrix power yields a non-zero entry between node  $i$  and node  $k$  if and only if there is at least one edge between  $i$  and  $j$  and one edge between  $j$  and  $k$ , where  $j$  is another node.

(2) *Short-time*: Assume  $\exp(-2t) > 1/2$ . The proof is nearly the same as in the previous case, where we have

$$\Sigma_t = \exp(-2t)\Sigma[I_V + c_t^{-1}\Sigma^{-1}],$$

which yields

$$\Sigma_t^{-1} = \exp(-2t)\left[\sum_{p=0}^{\infty} -c_t^{-p}\Sigma^{-(p+1)}\right].$$

The remaining steps are identical to above ones, where we use the  $v_2$ -locality of  $\Sigma^{-1}$  to establish the  $kv_2$ -locality of  $\Sigma_t^{-1}$ .  $\square$

## References

- Al-Shaalan, A. M. Reliability evaluation of power systems. 2019.
- Ardizzone, L., Kruse, J., Wirkert, S. J., Rahner, D., Pellegrini, E., Klessen, R. S., Maier-Hein, L., Rother, C., and Köthe, U. Analyzing inverse problems with invertible neural networks. *ArXiv*, abs/1808.04730, 2019a.
- Ardizzone, L., Lüth, C., Kruse, J., Rother, C., and Köthe, U. Guided image generation with conditional invertible neural networks. *arXiv preprint arXiv:1907.02392*, 2019b.
- Behrmann, J., Grathwohl, W., Chen, R. T., Duvenaud, D., and Jacobsen, J.-H. Invertible residual networks. In *International Conference on Machine Learning*, pp. 573–582. PMLR, 2019.
- Bolley, F., Gentil, I., and Guillin, A. Convergence to equilibrium in wasserstein distance for fokker–planck equations. *Journal of Functional Analysis*, 263(8):2430–2457, 2012.
- Cheng, X., Miao, Z., and Qiu, Q. Graph convolution with low-rank learnable local filters. In *International Conference on Learning Representations*, 2021.
- Clevert, D.-A., Unterthiner, T., and Hochreiter, S. Fast and accurate deep network learning by exponential linear units (elus). *arXiv preprint arXiv:1511.07289*, 2015.
- Defferrard, M., Bresson, X., and Vandergheynst, P. Convolutional neural networks on graphs with fast localized spectral filtering. *Advances in neural information processing systems*, 29, 2016.
- Dinh, L., Sohl-Dickstein, J., and Bengio, S. Density estimation using real nvp. *ArXiv*, abs/1605.08803, 2017.

- Goodfellow, I. J., Pouget-Abadie, J., Mirza, M., Xu, B., Warde-Farley, D., Ozair, S., Courville, A. C., and Bengio, Y. Generative adversarial nets. In *NIPS*, 2014.
- Grathwohl, W., Chen, R. T. Q., Bettencourt, J., Sutskever, I., and Duvenaud, D. K. Ffjord: Free-form continuous dynamics for scalable reversible generative models. *ArXiv*, abs/1810.01367, 2019.
- Gretton, A., Borgwardt, K. M., Rasch, M. J., Schölkopf, B., and Smola, A. A kernel two-sample test. *J. Mach. Learn. Res.*, 13:723–773, 2012.
- Gulrajani, I., Ahmed, F., Arjovsky, M., Dumoulin, V., and Courville, A. C. Improved training of wasserstein gans. In *NIPS*, 2017.
- Haykin, S. Neural networks: A comprehensive foundation. 1998.
- Ioffe, S. and Szegedy, C. Batch normalization: Accelerating deep network training by reducing internal covariate shift. *ArXiv*, abs/1502.03167, 2015.
- Isola, P., Zhu, J.-Y., Zhou, T., and Efros, A. A. Image-to-image translation with conditional adversarial networks. *2017 IEEE Conference on Computer Vision and Pattern Recognition (CVPR)*, pp. 5967–5976, 2017.
- Kingma, D. P. and Ba, J. Adam: A method for stochastic optimization. *CoRR*, abs/1412.6980, 2015.
- Kingma, D. P. and Welling, M. Auto-encoding variational bayes. *CoRR*, abs/1312.6114, 2014.
- Kingma, D. P. and Welling, M. An introduction to variational autoencoders. *Foundations and Trends® in Machine Learning*, 12(4):307–392, 2019. doi: 10.1561/22000000056.
- Kobyzev, I., Prince, S. J., and Brubaker, M. A. Normalizing flows: An introduction and review of current methods. *IEEE transactions on pattern analysis and machine intelligence*, 43(11): 3964–3979, 2020.
- Ledig, C., Theis, L., Huszár, F., Caballero, J., Aitken, A. P., Tejani, A., Totz, J., Wang, Z., and Shi, W. Photo-realistic single image super-resolution using a generative adversarial network. *2017 IEEE Conference on Computer Vision and Pattern Recognition (CVPR)*, pp. 105–114, 2017.
- Lu, J., Wu, D., Mao, M., Wang, W., and Zhang, G. Recommender system application developments: A survey. *Decis. Support Syst.*, 74:12–32, 2015.
- Lu, Z., Pu, H., Wang, F., Hu, Z., and Wang, L. The expressive power of neural networks: A view from the width. In *NIPS*, 2017.

- Lubotzky, A. Discrete groups, expanding graphs and invariant measures. In *Progress in mathematics*, 1994.
- Lucas, J., Tucker, G., Grosse, R. B., and Norouzi, M. Understanding posterior collapse in generative latent variable models. In *DGS@ICLR*, 2019.
- Makhzani, A., Shlens, J., Jaitly, N., and Goodfellow, I. J. Adversarial autoencoders. *ArXiv*, abs/1511.05644, 2015.
- Mirza, M. and Osindero, S. Conditional generative adversarial nets. *ArXiv*, abs/1411.1784, 2014.
- Newey, W. and McFadden, D. Large sample estimation and hypothesis testing. *Handbook of Econometrics*, 4:2111–2245, 1986.
- Salimans, T., Goodfellow, I. J., Zaremba, W., Cheung, V., Radford, A., and Chen, X. Improved techniques for training gans. *ArXiv*, abs/1606.03498, 2016.
- Sánchez-Lengeling, B. and Aspuru-Guzik, A. Inverse molecular design using machine learning: Generative models for matter engineering. *Science*, 361:360 – 365, 2018.
- Sideris, T. C. Ordinary differential equations and dynamical systems. 2013.
- Székely, G. J. and Rizzo, M. L. Energy statistics: A class of statistics based on distances. *Journal of Statistical Planning and Inference*, 143:1249–1272, 2013.
- Wehenkel, A. and Louppe, G. Unconstrained monotonic neural networks. *ArXiv*, abs/1908.05164, 2019.
- Xu, C., Cheng, X., and Xie, Y. Training neural networks using monotone variational inequality. *arXiv preprint arXiv:2202.08876*, 2022.
- Zhu, J.-Y., Park, T., Isola, P., and Efros, A. A. Unpaired image-to-image translation using cycle-consistent adversarial networks. *2017 IEEE International Conference on Computer Vision (ICCV)*, pp. 2242–2251, 2017.
- Ziegler, Z. M. and Rush, A. M. Latent normalizing flows for discrete sequences. In *ICML*, 2019.
- Zong, B., Song, Q., Min, M. R., Cheng, W., Lumezanu, C., ki Cho, D., and Chen, H. Deep autoencoding gaussian mixture model for unsupervised anomaly detection. In *ICLR*, 2018.

## A Additional experiments

### A.1 Setup details

1. *Verify model invertibility* We see from Figure 12 that iGNN under the Wasserstein-2 regularization ensures model invertibility up to very high accuracy.

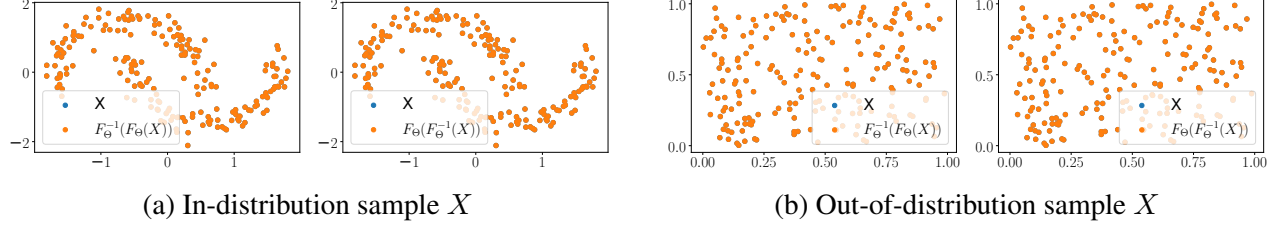


Figure 12: iGNN invertibility assessment. Given  $X$  and a fixed iResnet architecture, examine  $F_{\Theta}^{-1}(F_{\Theta}(X))$  (forward then invert) vs.  $F_{\Theta}(F_{\Theta}^{-1}(X))$  (invert then forward) on in-distribution data (two-moon) and out-of-distribution data (random  $U[0, 1]$  samples).

2. *Comparison methods* We compare iGNN with three conditional generative models, which are representative of different approaches to this task: the first builds on Generative Adversarial Network (GAN) (Goodfellow et al., 2014), the second uses invertible neural networks to analyze inverse problems (Ardizzone et al., 2019a), and the last extends the idea of normalizing flow (Ardizzone et al., 2019b). These works were originally developed for image generation tasks, but we apply them here due to the generality of these methods.

2.1. *Conditional Generative Adversarial Network (cGAN) (Isola et al., 2017)*: Denote  $Y \in [K]$  as the one-hot encoded categorical response,  $X_Y \in \mathbb{R}^n$  as the corresponding true feature, and  $Z \in \mathbb{R}^n$  as the random noise. Given a generator  $G : (Z, Y) \rightarrow \mathbb{R}^n$  and a discriminator  $D : (X_Y, Y) \rightarrow [0, 1]$ , the objective of the cGAN loss is

$$\arg \min_G \max_D \mathcal{L}_{cGAN}(G, D) + \lambda \mathcal{L}_2(G) \quad (16)$$

$$\mathcal{L}_{cGAN}(G, D) := \mathbb{E}_{X_Y, Y}[\log D(X_Y, Y)] + \mathbb{E}_{Z, Y}[\log(1 - D(G(Z, Y), Y))] \quad (17)$$

$$\mathcal{L}_2(G) := \mathbb{E}_{X_Y, Z, Y}[\|X_Y - G(Z, Y)\|_2] \quad (18)$$

We note that the discriminator  $D$  aims to maximize (17) in order to distinguish fake features  $G(Z, Y)$  from the true ones  $X_Y$ , whereas the generator  $G$  tries to fool  $D$  by minimizing (17). Therefore, this min-max game leads to objective (16), which also includes an  $\ell_2$  penalty to force  $G$  producing features as similar to  $X_Y$  as possible.

During maximization, we adopt the recommendation in (Isola et al., 2017; Goodfellow et al., 2014) by training  $G$  to maximize  $\mathbb{E}_{Z, Y}[\log D(G(Z, Y), Y)]$ . We also divide the objective by 2 when

optimizing  $D$ , so as to slow down the rate it learns comparing to  $G$ .

We adopt the following hyperparameters and model architectures upon visual cross-validation (i.e., comparing the generative performances). Regarding architecture, we aim to use networks as similar to our iGNN as possible for fair comparisons. In particular, we concatenate blocks of layers together but do not restrict the output of each block, as we need not worry about model invertibility; a batch normalization layer (Ioffe & Szegedy, 2015) is used after each block. Because cGAN is not flow-based, we keep the hidden dimension of all except the last layer in the last block at 64, rather than forcing the output of each block to lie within the original dimension (as when training our iGNN). In practice, the generative task seems harder than the discriminative task, so we always make  $G$  twice deeper as  $D$ , with the former having 40 blocks. Regarding hyperparameters, we fix  $\lambda = 5$  in (16) and always use the Adam optimizer under weight decay equal to 0.5 (i.e.,  $l_2$  penalty on model parameters). The learning rates for network  $G$  and network  $D$  are fixed as (a)  $5e-4$  and  $1e-4$  for generating 2D convex node features and the solar anomaly detection (b)  $1e-1$  and  $1e-3$  for the traffic anomaly detection. All other hyperparameters (e.g., structure of each block, batch size, termination criteria, etc.) are the same as we did in our training of (16).

**2.2. Conditional Invertible Neural Networks with Maximum Mean Discrepancy (CINN-MMD)** (Ardizzone et al., 2019a): This method constructs conditional coupling blocks as follows. Denote  $Y$  as one-hot encoded categorical feature and  $X_b$  as the input to the  $b$ -th block  $f_b$ , which first splits  $X_b$  into two parts  $[X_{b,1}, X_{b,2}]$ . Then, the output by  $f_b$  is  $[X_{b+1,1}, X_{b+1,2}]$ , where

$$\begin{aligned} X_{b+1,1} &= X_{b,1} \odot \exp(s_{b,1}(X_{b,2}, Y)) + t_{b,1}(X_{b,2}, Y), \\ X_{b+1,2} &= X_{b,2} \odot \exp(s_{b,2}(X_{b+1,1}, Y)) + t_{b,2}(X_{b+1,1}, Y), \end{aligned} \quad (19)$$

where the subnetworks  $\{s_{b,1}, s_{b,2}, t_{b,1}, t_{b,2}\}$  can be arbitrary neural networks. The full network  $f := f_B \circ \dots \circ f_1$  thus concatenates  $B$  such blocks and takes in input  $X_0 = X$  and outputs  $X_B$ .

Given a CINN as the concatenation of  $B$  blocks, the method optimizes the following three losses where  $Z$  follows a standard multivariate Gaussian:

$$\begin{aligned} \mathcal{L}_Y &:= \mathbb{E}[(Y - f_Y(X))^2,] \\ \mathcal{L}_Z &:= D(q(Y, Z), p(Y)p(Z)), \\ \mathcal{L}_X &:= D(q(X), p(X)). \end{aligned}$$

Note that (1)  $\mathcal{L}_y$  measures the prediction error between true  $Y$  and  $f_Y(X)$ , where  $f(X) = [f_Y(X), f_Z(X)]$  denotes the full prediction. (2)  $\mathcal{L}_Z$  (resp.  $\mathcal{L}_X$ ) measures the distance between the

joint distribution of  $(Y, Z)$  based on prediction (resp. the distribution based on generated samples) and the product of their true marginal distributions (resp. true distribution of  $X$ ). The notation  $q$  denotes the estimated distribution based on  $f(X)$  and  $p$  denotes the true distribution for variables  $Y$  and  $Z$ . The distance function  $D$  is chosen as the MMD distance under the Inverse Multiquadratic kernel. In addition to this setup, (Ardizzone et al., 2019a) suggested several tricks during optimization and model construction, including blocking the gradient of  $\mathcal{L}_Z$  with respect to  $Y$ , balancing the effect of three losses, and random shuffling of hidden variables.

We adopt the following hyperparameters and model architectures upon visual cross-validation (i.e., comparing the generative performances). Regarding architecture, 40 blocks are used, and each subnetwork has three FC layers with hidden dimensions fixed at 128; we did not use a graph filter because of the splitting of features at each block. Splitted features are always assumed to have the same dimension. Regarding hyperparameters, we fix  $\lambda = 0.5$  in (16) and always use the Adam optimizer with learning rate at  $5e-4$ . All other hyperparameters (e.g., batch size, termination criteria, etc.) are the same as we did in our training of (16).

*2.3. Conditional Invertible Neural Networks with Normalizing Flow (CINN-Nflow) (Ardizzone et al., 2019b):* Given a CINN as the concatenation of  $B$  blocks, the method directly optimizes the unconditional generative loss in (4) using  $X_B$ . It also adds an  $\ell_2$  weight regularization for better practical performance. The construction of the conditional coupling blocks is identical to CINN-MMD, so that we omit the descriptions. The same hyperparameters as used earlier are also adopted.

## A.2 Further results

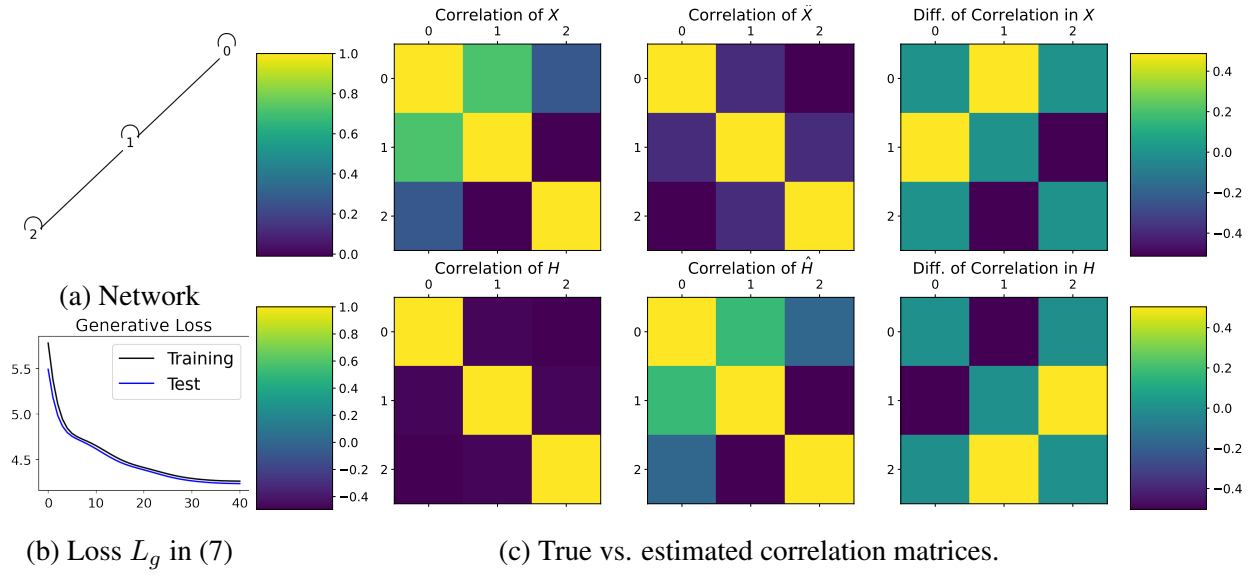


Figure 13: IGNN results for the local  $\Sigma$  as in Proposition 3.8. Each residual block in iGNN is the Chebnet. We see that losses converge reasonably fast, but correlation matrices are not estimated well, revealing the effect of GNNs lacking expressiveness in generative tasks. This example contrasts with iGNN under L3net in Figure 11c, which shows satisfactory generative performances when GNN has enough expressiveness.



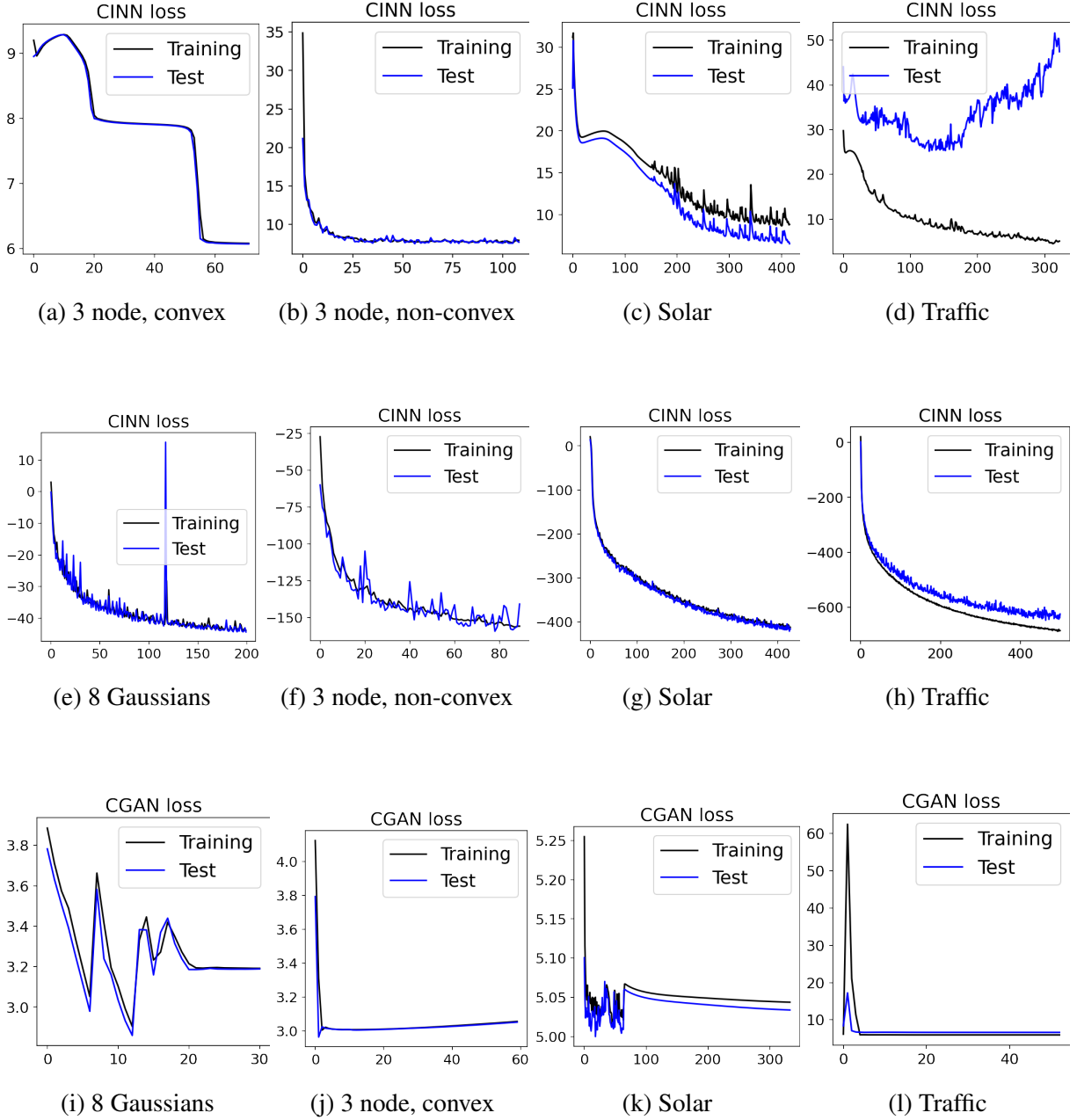


Figure 14: Losses by competing methods on simulated and real-data experiments. We see that losses all converges but generative performance differs. First row: losses for CINN-MMD. Second row: losses for CINN-Nflow. Last row: losses for cGAN

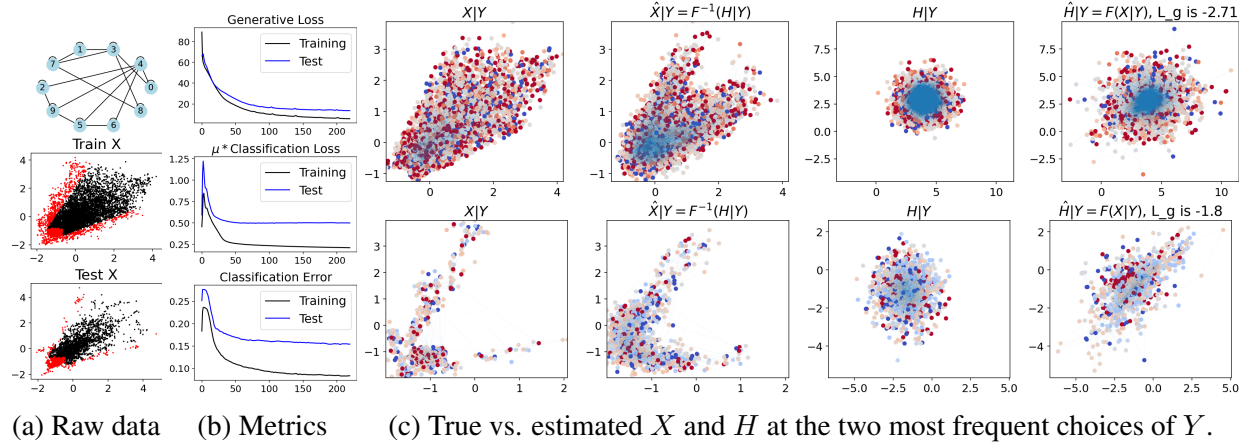


Figure 15: CA solar ramping event detection. We replace in iGNN the Chebnet layer with an L3net layer and show the network and raw features in (a), loss and error metrics in (b), and generative performances of the 20-dimensional node feature matrices in (c). The generative performances are similar to the ones in Figure 7.

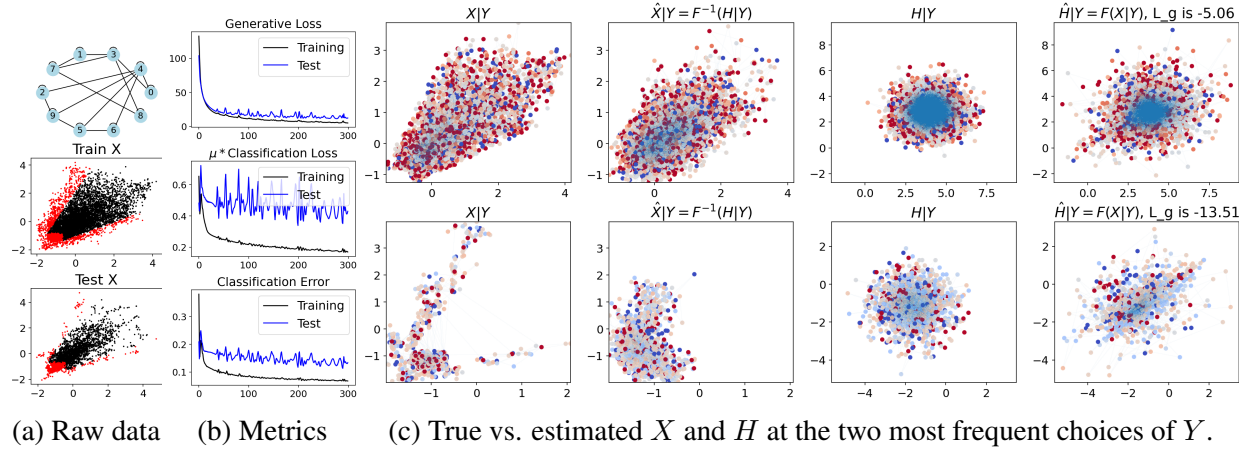


Figure 16: CA solar ramping event detection by using FC layers in iGNN only. We show the network and raw features in (a), loss and error metrics in (b), and generative performances of the 20-dimensional node feature matrices in (c). The generative performances are poorer than the earlier ones in Figure 7 and 15.

Table 6: Solar ramping event, two-sample testing statistics at each  $X|Y$  before weighting. The first column indicates the outcome of  $Y$  on the graph and the number of graph observations in the data. We see that our method has very similar test statistics as CINN-MMD, but the statistics can have too much variance when samples are too few, where it is essential to examine the generative performances qualitatively as we did in Figure 7.

Training		iGNN	CINN-MMD	CINN-Nflow	cGAN
$Y = (0,0,0,0,0,0,0,0,0,0)$ , 679 obs	MMD: $\alpha=0.1$	0.041	0.021	0.304	0.267
	MMD: $\alpha=1.0$	0.081	0.086	0.582	1.297
	MMD: $\alpha=5.0$	0.231	0.210	0.197	0.668
	MMD: $\alpha=10.0$	0.019	0.017	0.040	0.800
	Energy	0.123	0.146	0.201	1.201
$Y = (1,1,1,1,1,1,1,1,1,1)$ , 144 obs	MMD: $\alpha=0.1$	0.038	0.031	0.027	1.026
	MMD: $\alpha=1.0$	0.004	0.004	0.004	0.974
	MMD: $\alpha=5.0$	0.041	0.046	0.047	1.047
	MMD: $\alpha=10.0$	0.009	0.009	0.009	1.009
	Energy	0.002	0.002	0.002	0.992
$Y = (0,0,0,0,0,0,0,0,1,0)$ , 22 obs	MMD: $\alpha=0.1$	0.020	0.021	0.021	1.021
	MMD: $\alpha=1.0$	0.004	0.004	0.004	1.004
	MMD: $\alpha=5.0$	0.189	0.075	2.418	1.895
	MMD: $\alpha=10.0$	0.387	0.632	5.221	6.288
	Energy	1.485	1.106	2.850	3.425
Test		iGNN	CINN-MMD	CINN-Nflow	cGAN
$Y = (0,0,0,0,0,0,0,0,0,0)$ 222 obs	MMD: $\alpha=0.1$	0.029	0.014	0.286	0.334
	MMD: $\alpha=1.0$	0.150	0.172	0.774	1.380
	MMD: $\alpha=5.0$	0.281	0.446	0.798	1.084
	MMD: $\alpha=10.0$	0.013	0.010	0.032	0.831
	Energy	0.207	0.199	0.274	1.273
$Y = (1,1,1,1,1,1,1,1,1,1)$ 59 obs	MMD: $\alpha=0.1$	0.311	0.239	0.331	1.327
	MMD: $\alpha=1.0$	0.002	0.002	0.003	0.980
	MMD: $\alpha=5.0$	0.048	0.050	0.051	1.051
	MMD: $\alpha=10.0$	0.066	0.063	0.066	1.066
	Energy	0.001	0.001	0.001	0.993
$Y = (1,0,1,1,1,1,1,1,1,1)$ 10 obs	MMD: $\alpha=0.1$	0.021	0.021	0.021	1.021
	MMD: $\alpha=1.0$	0.025	0.025	0.025	1.025
	MMD: $\alpha=5.0$	0.200	0.145	2.646	2.422
	MMD: $\alpha=10.0$	0.677	0.799	6.374	6.877
	Energy	1.483	2.072	5.146	5.230